Suppression of p16 increases nucleotide synthesis via mTORC1

Raquel Buj[1], Chi-Wei Chen[1], Erika S. Dahl[1], Kelly E. Leon[1], Ross Kuskovsky[2], Natella Maglakelidze[3], Maithili Navaratnarajah[1], Gao Zhang[4], Mary T. Doan[2], Helen Jiang[2], Michael Zaleski[5], Lydia Kutzler[1], Holly Lacko[1], Yiling Lu[6], Gordan B. Mills[7], Raghavendra Gowda[8], Gavin P. Robertson[8], Joshua I. Warrick[5], Meenhard Herlyn[4], Yuka Imamura[8], Scot R. Kimball[1], David J. DeGraff[5], Nathaniel W. Snyder[2], and Katherine M. Aird[1*]

[1] Department of Cellular & Molecular Physiology, Penn State College of Medicine, Hershey, PA, USA

[2] A.J. Drexel Autism Institute, Drexel University, Philadelphia, PA, USA

[3] MSTP Program, Penn State College of Medicine, Hershey, PA, USA

[4] Molecular and Cellular Oncogenesis Program and Melanoma Research Institute, The Wistar Institute, Philadelphia, PA, USA

[5] Department of Pathology, Penn State College of Medicine, Hershey, PA, USA

[6] Department of Systems Biology, The University of Texas MD Anderson Cancer Center, Houston, TX, USA

[7] Department of Cell, Developmental & Cancer Biology, Oregon Health and Sciences University, Portland, OR, USA

[8] Department of Pharmacology, Penn State College of Medicine, Hershey, PA, USA

[*] Lead contact
Katherine M. Aird
Assistant Professor
Department of Cellular & Molecular Physiology
Penn State College of Medicine
Hershey, PA
717 531 5014
kaird@psu.edu

Summary

Reprogrammed metabolism and cell cycle dysregulation are two cancer hallmarks. p16 is a cell cycle inhibitor and tumor suppressor that is upregulated during oncogene-induced senescence (OIS). Loss of p16 allows for uninhibited cell cycle progression, bypass of OIS, and tumorigenesis. Whether p16 loss affects pro-tumorigenic metabolism is unclear. We report that suppression of p16 plays a central role in reprogramming metabolism by increasing nucleotide synthesis. This occurred via Ataxia Telangiectasia and Rad3-Related Protein (ATR) activation of mTORC1 signaling, which mediated increased translation of the mRNA encoding ribose-5-phosphate isomerase A (*RPIA*), a pentose phosphate pathway enzyme. p16 loss correlated with activation of the ATR-mTORC1-RPIA axis in multiple cancer types. Suppression of RPIA inhibited proliferation of cancer cells only with low p16 by inducing senescence both *in vitro* and *in vivo*. These data reveal the molecular basis whereby p16 loss modulates pro-tumorigenic metabolism through mTORC1-mediated upregulation of nucleotide synthesis and reveals a metabolic vulnerability of p16-low cancer cells.

Keywords

Cancer metabolism, RRM2, cell cycle, senescence, melanoma, pancreatic cancer, nevi, replication stress, ATR, pentose phosphate pathway, ribose-5-phosphate isomerase A

Highlights

- Suppression of p16 activates the ATR-mTORC1 signaling axis to increase nucleotide synthesis
- Low p16 expression increases sensitivity to mTORC1 inhibition
- mTORC1 increases translation of the mRNA encoding the pentose phosphate pathway enzyme ribose-5-phosphate isomerase A (RPIA)
- RPIA suppression induces senescence only in cancer cells with low p16

Introduction

Metabolic reprogramming is considered a hallmark of cancer (Hanahan and Weinberg, 2011; Pavlova and Thompson, 2016). Transformed and tumorigenic cells require increased deoxyribonucleotide synthesis for replication of their genome to sustain the unregulated cell cycle and proliferation observed. Therefore, it is likely that the cell cycle and nucleotide metabolism are linked. p16 is a cell cycle inhibitor and critical tumor suppressor that is lost as an early event in many human cancers (Belinsky et al., 1998; Chin, 2003; Hruban et al., 2000; Nuovo et al., 1999). p16 expression is low in approximately half of all human cancers (Li et al., 2011). This mostly occurs through homozygous deletion or DNA methylation and loss of heterozygosity (LOH) (Merlo et al., 1995; Ortega et al., 2002). The Cancer Genome Atlas (TCGA) shows 24% of melanomas and 28% of pancreatic cancers harbor homozygous deletions in cyclin dependent kinase inhibitor (*CDKN2A,* encoding for p16) (Cerami et al., 2012; Gao et al., 2013; Shain et al., 2018; Shain et al., 2015). In other cancers, such as colorectal cancers, *CDKN2A* is often silenced by promoter hypermethylation (12-51% of cases) (Herman et al., 1995; Shima et al., 2011). While loss of p16 is known to play a role in deregulating the cell cycle, whether loss of p16 expression affects nucleotide metabolism is unknown.

Cellular senescence is a metabolically active state of cell cycle arrest (Aird and Zhang, 2014, 2015; Dorr et al., 2013; Hernandez-Segura et al., 2018; Wiley and Campisi, 2016). Activation of oncogenes induces senescence to suppress transformation and tumorigenesis (termed oncogene-induced senescence, OIS) (Perez-Mancera et al.,

2014; Yaswen and Campisi, 2007). Therefore, OIS is considered an important tumor suppressor mechanism *in vivo* (Braig et al., 2005; Michaloglou et al., 2005). OIS is characterized by both a depletion in deoxyribonucleotide levels (Aird et al., 2013; Mannava et al., 2013) and increased expression of p16 (Serrano et al., 1997). Increased deoxyribonucleotide triphosphates (dNTPs) or loss of p16 bypasses OIS to allow for transformation and tumorigenesis (Aird et al., 2015; Aird et al., 2013; Damsky et al., 2015; Dankort et al., 2007; Goel et al., 2009; Haferkamp et al., 2008; Sarkisian et al., 2007). Thus, we reasoned that these two processes may be interconnected.

We probed the role of p16 loss in nucleotide metabolism by utilizing a senescence model based on inhibition of deoxyribonucleotide synthesis. We previously established that suppression of ribonucleotide reductase M2 (RRM2), which reduces NDPs/NTPs to dNDPs/dNTPs and is rate-limiting for deoxyribonucleotide synthesis, is sufficient to induce robust replication stress, accumulation of DNA damage, and senescence (Aird et al., 2013). Here, we report that depletion of p16 increases deoxyribonucleotide synthesis to bypass senescence induced by RRM2 suppression. Mechanistically, this is due to Ataxia Telangiectasia and Rad3-Related Protein (ATR)-mediated increased mTORC1 activation. Activation of mTORC1 in turn increases translation of ribose-5-phosphate isomerase A (*RPIA*), an enzyme in the pentose phosphate pathway (PPP) that is important for synthesis of the ribose sugar for both purines and pyrimidines (Patra and Hay, 2014). Underscoring the importance of this pathway in human cancers, Chk1 and mTORC1 activation correlate with p16 expression and worse prognosis in multiple cancer types. Finally, cancer cells with low p16 expression are more sensitive to the mTORC1

inhibitor temsirolimus and rely upon RPIA expression for proliferation both *in vitro* and *in vivo*. These data demonstrate that loss of p16 increases deoxyribonucleotide synthesis through upregulation of mTORC1 activity.

Results

p16 knockdown enhances nucleotide synthesis to bypass senescence

We previously published that increased dNTP levels bypass senescence (Aird et al., 2013). p16 is upregulated during oncogene-induced senescence (Braig et al., 2005; Collado and Serrano, 2010; Michaloglou et al., 2005). Loss of p16 may be an early event in the progression from senescent benign lesions to cancer (Bennecke et al., 2010; Bennett, 2016; Caldwell et al., 2012; Kriegl et al., 2011; Michaloglou et al., 2005; Shain et al., 2015). It is unknown whether p16 regulates nucleotide synthesis in this context. By cross-referencing two publicly available datasets (Kabbarah et al., 2010; Talantov et al., 2005), we found that nucleotide synthesis pathways are enriched in human melanoma samples compared to benign nevi, which are considered senescent (**Fig. 1A**) (Michaloglou et al., 2005). Therefore, we aimed to determine whether p16 loss affects nucleotide synthesis. Senescence due to nucleotide depletion was induced by knocking down ribonucleotide reductase M2 (RRM2) (**Fig 1B**) (Aird et al., 2013), the rate-limiting enzyme in *de novo* deoxyribonucleotide synthesis by reducing NDPs to dNDPs (Nordlund and Reichard, 2006). We have previously extensively validated this short hairpin RNA (shRNA) (Aird et al., 2013). As expected, shRRM2 cells had ~50% less dNDPs (**Fig. 1C**) and dNTPs (**Fig. S1A**) than control cells. Note that dGDP/dGTP was not quantified due to spectral overlap with the higher abundance ADP/ATP. Knockdown of p16 in shRRM2 cells (**Fig. 1B and S1B**) significantly increased dNDPs/dNTPs even above control levels in both pyrimidine dNDPs (**Fig. 1C**). This correlated with a suppression of senescence markers including BrdU incorporation, colony forming ability, and senescence-associated beta-galactosidase (SA-β-Gal) activity (**Fig. 1D-I**). These cells are termed “senescent

bypassed". Overexpression of p16 cDNA rescued senescence bypass (**Fig. S1C-I**), suggesting that this hairpin is specific for p16. Additionally, senescence bypass was observed using a second independent hairpin to p16 (**Fig. S1J-N**).

Cells require 10-20 times more dNTPs in S-phase (Hakansson et al., 2006). However, the increase in deoxyribonucleotides observed in senescent bypassed cells was not due to an increased proportion of these cells in S-phase (**Fig. S1O**). This suggests that the increase in deoxyribonucleotides observed is not simply due to increased dNTP demand during S-phase. Additionally, nucleotide diphosphates were also increased in senescent bypassed cells (**Fig. S1P**), suggesting that the increase in deoxyribonucleotides is not due to compensatory upregulation of other ribonucleotide reductase (RNR) subunits. To determine whether the increase in deoxyribonucleotide synthesis occurred through the *de novo* or salvage pathway, we inhibited *de novo* nucleotide synthesis using 3-aminopyridine-2-carboxaldehyde thiosemicarbazone (3AP) as we have previously published (Aird et al., 2015). 3AP inhibits both R2 subunits of RNR (RRM2 and RRM2B) to suppress the reduction of NDPs to dNDPs in the *de novo* pathway (Finch et al., 2000; Finch et al., 1999). Knockdown of p16 did not rescue senescence due to 3AP treatment (**Fig. S1Q-T**). This suggests that the observed increase in nucleotides is via the *de novo* pathway. Additionally, these data indicate that RRM2B, the other R2 subunit of RNR, is necessary for the reduction of the increased nucleotides observed during senescence bypass. Together, these data indicate that p16 depletion increases dNTP synthesis via the *de novo* pathway to bypass senescence.

p16 knockdown activates mTORC1 to increase nucleotide synthesis

We next aimed to determine the underlying mechanism of *de novo* nucleotide synthesis in senescent bypassed cells due to p16 knockdown. p16 inhibits E2F-mediated transcription in part through regulating the retinoblastoma protein (pRb)-E2F interaction (Sherr, 2001). Therefore, we performed an RNA-Seq analysis to determine whether changes in transcription of enzymes involved in nucleotide synthesis account for the increased deoxyribonucleotide levels. Surprisingly, Gene Set Enrichment Analysis (GSEA) terms related to nucleotide biosynthesis were not enriched in p16 knockdown senescent bypassed cells compared to senescent cells. However, Translation and Metabolism of RNA GSEA terms were significantly enriched in p16 knockdown senescent bypassed cells (**Table S1**). Additionally, mTOR signaling, a master regulator of translation and mRNA metabolism (Ma and Blenis, 2009; Nandagopal and Roux, 2015), was one of the top hits in a reverse phase protein array (RPPA) analysis (**Fig. 2A**). mTORC1 increases both purine and pyrimidine synthesis (Ben-Sahra et al., 2013; Ben-Sahra et al., 2016). To determine whether mTORC1 signaling correlated with increased nucleotide levels in senescent bypassed cells, we performed western blotting for phosphorylated S6K, which is downstream of mTORC1 (Magnuson et al., 2012). S6K was highly phosphorylated in senescent bypassed cells (**Fig. 2B**). mTORC1/LAMP2 co-localization further demonstrated that mTORC1 activity is upregulated in p16 knockdown senescent bypassed cells (**Fig. S2A**). Similar results were also observed in senescence bypass by p16 knockdown in a $BRAF^{V600E}$ model (**Fig. S2B**). This is consistent with previous data in a *CDKN2A* knockout mouse model of melanomagenesis (Damsky et al., 2015). Interestingly, knockdown of pRb suppressed senescence but did not increase p-S6K (**Fig.**

S2C-J). Similar results were observed using a publicly-available dataset of pRb knockdown in senescence (**Table S2**) (Chicas et al., 2010). This suggests that the upregulation of mTORC1 activity is due to a non-canonical pathway downstream of p16 loss. Importantly, these results also indicate that the increase in mTORC1 activity is not a cell cycle-dependent phenomenon. Activation of mTORC1 was necessary for p16 knockdown-induced suppression of senescence due to deoxyribonucleotide depletion as pharmacological inhibition of mTORC1 with temsirolimus reversed this phenotype (**Fig. 2B-H**). Temsirolimus had no effect on parental cell proliferation (**Fig. S2K**), suggesting this effect is specific for senescent bypassed cells with high mTORC1 activity. Finally, mTORC1 activity was also necessary for deoxyribonucleotide synthesis upon p16 knockdown as treatment of senescent bypassed cells with temsirolimus suppressed both purine and pyrimidine deoxyribonucleotide levels (**Fig. 2I**). Together, these results indicate that p16 knockdown increases deoxyribonucleotide synthesis in a non-canonical pathway via mTORC1.

ATR activates mTORC1 to increase nucleotide synthesis

Replication stress, DNA damage, and the associated DNA damage response (DDR) are hallmarks of senescence (Aird et al., 2015; Aird et al., 2013; Bartkova et al., 2006; Di Micco et al., 2006). We previously published that increased dNTP levels rescue the replication stress and DNA damage accumulation observed during senescence (Aird et al., 2015; Aird et al., 2013). mTORC1 activity is intricately related to the DDR (Ma et al., 2018). Therefore, we aimed to determine whether mTORC1-mediated dNTP synthesis mitigates replication stress and subsequent DNA damage accumulation induced by

RRM2 knockdown. RNA-Seq analysis indicates that DNA repair pathway activation is increased in senescent bypassed cells due to p16 knockdown (**Fig. S3A**), which correlates with mTORC1 activity (**Fig. 2B**). Indeed, we observed an increased phosphorylation of the ATR downstream effector Chk1 (checkpoint kinase 1) in senescent bypassed cells due to p16 knockdown (**Fig. 3A**). No difference was observed in the phosphorylation of the ATM (ataxia telangiectasia mutated) downstream effector Chk2 (checkpoint kinase 2) (**Fig. S3B**). This is consistent with the idea that mild activation of the ATR-Chk1 signaling pathway may mitigate replication stress and DNA damage to allow for proliferation (Lecona and Fernandez-Capetillo, 2014; Lopez-Contreras et al., 2012). Indeed, ATR-Chk1 signaling is upregulated in multiple human cancers (Lecona and Fernandez-Capetillo, 2014), and analysis of melanoma samples shows that this pathway is upregulated in melanoma samples compared to senescent benign nevi (**Fig. S3C**). Consistent with the notion that mTORC1 activation is independent of pRb (**Fig. S2J**), knockdown of pRb did not increase p-Chk1 (**Fig. S3D**). Together, these data suggest that the ATR-mTORC1 signaling axis is necessary for bypassing senescence due to p16 knockdown.

A previous study showed that loss of mTORC1 signaling decreases p-Chk1 (Zhou et al., 2017). To determine whether mTORC1 is upregulating Chk1 phosphorylation in p16 knockdown senescent bypassed cells, we treated cells with the mTORC1 inhibitor temsirolimus. Surprisingly, inhibition of mTORC1 activity had no effect on p-Chk1 levels (**Fig. 3B**). This suggests that ATR-Chk1 signaling may instead act upstream of mTORC1. To delineate this possibility, we treated senescence bypassed cells with VE822, a specific

ATR inhibitor. Inhibition of ATR, as indicated by a decrease in p-Chk1, decreased S6K phosphorylation (**Fig. 3A**). Inhibition of ATR signaling phenocopied inhibition of mTORC1, as shown by reversal of senescence bypass (**Fig. 3C-H**). VE822 had no effect on parental cell proliferation (**Fig. S3E**). Finally, inhibition of ATR correlated with decreased dNTP levels (**Fig. 3I**). Together, these data indicate that ATR activates mTORC1 downstream of p16 depletion during senescence bypass. ATR is a protein kinase that is directly activated by DNA replication stress and single strand breaks (Saldivar et al., 2017). Phosphoproteomic analysis indicates that ATR may directly phosphorylate TSC1 (Matsuoka et al., 2007). Phosphorylation of TSC1 would in turn activate mTORC1 (Lee et al., 2007; Li et al., 2018). While it is mostly nuclear, multiple recent publications have shown a small fraction of ATR in the cytoplasm (Hilton et al., 2016; Postigo et al., 2017). We found that ATR abundance in the cytoplasmic fraction is greater in senescent bypassed cells compared to senescent cells (**Fig. S3F**). To determine whether ATR colocalizes with TSC1, we performed confocal immunofluorescence of ATR and TSC1. We observed an increase in colocalization between ATR and TSC1 in the cytoplasm of senescent bypassed cells compared to control cells (**Fig. S3G-H**). Knockdown of ATR decreased cytoplasmic staining and TSC1 co-localization (**Fig. S3I-J**). Taken together, these data suggest cytoplasmic ATR potentially activates mTORC1-mediated nucleotide synthesis through TSC1.

ATR-mTORC1 signaling axis is a therapeutic vulnerability in p16-low cancer cells

p16 expression is lost in multiple human cancers. Therefore, we next aimed to determine whether p16 expression status correlates with activation of the ATR-mTORC1 pathway

in cancer cells. We observed a trend towards a correlation between p16 expression and S6K and Chk1 phosphorylation in multiple cell lines with BRAF and KRAS mutations from a diverse set of human cancers (melanoma, pancreatic, colon, and ovarian) (**Fig. 4A-B and S4A**). Two of the cell lines with the highest *CDKN2A* expression (ES2 and HT-29) show very low expression of both pS6K and pChk1, whereas those with the lowest *CDKN2A* expression (MelJuSo and Hupt4) show the highest pS6K and pChk1 expression (**Fig. 4B**). Knockdown of p16 in isogenic cell lines from multiple human cancers (**Fig. S4B**) upregulated p-S6K and p-Chk1 expression (**Fig. 4C**). Analysis of data from the Dependency Map (depmap.org) indicates that low p16 copy number correlates with sensitivity to temsirolimus and the Chk inhibitor AZD7726 (**Fig. S4C-D**), and knockdown of p16 in p16-high cancer cells also increased sensitivity to temsirolimus (**Fig. 4D**). Finally, there is a positive correlation between sensitivity to temsirolimus and AZD7762 (**Fig. 4E**). Interestingly, increased expression of leading-edge genes associated with "translation" and "DNA repair" GSEA terms (**Table S4**) leads to worse overall survival of melanoma, pancreatic, lung, and colorectal cancer patients harboring a mutation in BRAF, NRAS, or KRAS (**Fig. 4F**) (Cerami et al., 2012; Gao et al., 2013). Together, these data suggest that the ATR-mTORC1 pathway is further activated in cancer cells and human tumors with low p16, and activation of this pathway leads to both increased sensitivity to inhibition of mTORC1 and with a worse prognosis.

mTORC1 activation by p16 knockdown increases translation of ribose-5-phosphate isomerase A to promote nucleotide synthesis

We did not observe GSEA terms involving nucleotide synthesis in p16 knockdown senescent bypassed cells by RNA-Seq (**Table S1**). Previous reports have shown that mTORC1 upregulates purine and pyrimidine metabolism through ATF4-*MTHFD2* and CAD, respectively (Ben-Sahra et al., 2013; Ben-Sahra et al., 2016). We did not observe an increase in transcription of *MTHFD2* (**Fig. S5A**), suggesting that this mechanism does not explain the increased purine synthesis observed in senescent bypass due to p16 suppression. Additionally, there was no difference in CAD phosphorylation between senescent and senescent bypassed cells (**Fig. S5B**). These data suggest an alternative mechanism is regulating nucleotide synthesis downstream of mTORC1 in senescent bypassed cells with p16 knockdown. mTORC1 activity increases translation (Ma and Blenis, 2009); therefore, we aimed to determine whether the observed increase in mTORC1-mediated nucleotide synthesis in senescent bypassed cells due to p16 knockdown increases translation of transcripts involved in nucleotide synthesis. Towards this goal, we performed polysome fractionation (**Fig. S5C**) followed by qRT-PCR analysis of transcripts involved in purine and pyrimidine synthesis and related anaplerotic pathways (**Table S3**). The positive control *EEF2* was increased in the heavy polysome fraction in senescent bypassed cells (**Fig. S5D**), which correlates with mTORC1 activity (i.e., **Fig. 2B**). Our results reveal a number of transcripts whose abundance is upregulated in the heavy polysome fraction and downregulated in the light polysome fraction (**Fig. 5A and Table S3**), suggesting that these are translationally upregulated during senescence bypass due to p16 knockdown. We decided to focus only on those transcripts that were significantly upregulated in the heavy fraction and downregulated in the light fraction in senescent bypassed cells. Additionally, both purines and pyrimidines were increased in

senescence bypassed cells due to p16 knockdown (i.e., **Fig. 1C**) through the *de novo* pathway (**Fig. S1Q-T**). Thus, we further narrowed the list to those transcripts that play an important role in both *de novo* purine and pyrimidine nucleotide synthesis. Using these criteria, we narrowed the list down to two "hits": ribose-5-phosphate isomerase A (RPIA) and nucleoside diphosphate kinase A (NME1) (**Fig. 5A**). NME1 is a known metastasis suppressor (Boissan et al., 2018); therefore, we focused on RPIA (**Fig. 5B**). Increased protein expression of RPIA in senescent bypassed cells was confirmed by western blotting (**Fig. 5C**). Inhibition of either ATR or mTORC1 suppressed RPIA expression (**Fig. 5C**). RPIA is an enzyme that catalyzes one of the possible first steps of the non-oxidative branch of the pentose phosphate pathway (PPP). This step reversibly isomerizes D-ribulose 5-phosphate produced from the oxidative branch of the PPP to D-ribose-5-phosphate, which forms the ribose sugar backbone of both purine and pyrimidine nucleotides (Lane and Fan, 2015). Consistent with increased RPIA expression, the PPP metabolite ribose-5-phosphate (R5P) was increased in senescent bypassed cells and decreased by inhibition of either ATR or mTORC1 (**Fig. 5D**). Consistently, patient tumors with low p16 displayed high R5P levels (**Fig. S5E-F**). To determine whether RPIA enzyme is critical for senescence bypass by p16 knockdown, we depleted RPIA using two independent shRNAs. Our data indicate that RPIA is necessary for senescence bypass after p16 knockdown as shown by the reversal of this phenotype (**Fig. 5E-K**). Knockdown of RPIA alone had no effect on parental cells (**Fig. S5G-M**). To determine whether the PPP is responsible for the increased nucleotides observed in senescent bypassed cells (e.g., **Fig. 1C**), we performed stable isotope labeling using U-^{13}C glucose. Indeed, there was an increase in M+5 glucose labeling of dTTP in senescent bypassed cells due to p16

knockdown (**Fig. 5L**), which strongly suggests increased incorporation of PPP metabolites into the ribose backbone of dNTPs. Inhibition of ATR or mTORC1 suppressed M+5 labeling of dTTP (**Fig. 5L**). Taken together, these data demonstrate that increased mTORC1-mediated translation of RPIA is critical for senescence bypass due to p16 loss by increasing PPP activity and nucleotide synthesis.

Suppression of ribose-5-phosphate isomerase A limits proliferation of cancer cells with low p16 by inducing senescence

Low p16 expression correlates with activation of the ATR-mTORC1 pathway in cancer cell lines (**Fig. 4B**). Since mTORC1 increased RPIA translation (**Fig. 5A-B**), we next aimed to determine whether p16 expression also correlates with RPIA expression. We observed a trend towards a correlation between p16 expression and RPIA expression in multiple cancer cell lines (**Fig. S6A-B**). Additionally, knockdown of p16, which increased ATR-mTORC1 signaling (**Fig. 4C**) also increased RPIA expression in 7 different isogenic cancer cell lines (**Fig. 6A**). To determine whether low p16 expression creates a vulnerability to RPIA inhibition, we knocked down p16 in multiple cancer cell lines with high p16 expression (**Fig. S4B**) and simultaneously knocked down RPIA (**Fig. 6B and S6C**). Knockdown of RPIA in combination with p16 knockdown reverted cells to a senescent state as shown by markers of senescence such as increase cytoplasm and flat morphology, increased SA-β-Gal activity, decreased *CCNA2*, and decreased *LMNB1* (**Fig. 6C-D and S6D-E**). Finally, the cell cycle arrest was confirmed by decreased BrdU incorporation and colony formation (**Fig. 6C and S6D**). However, knockdown of RPIA alone did not affect cancer cell senescence or proliferation (**Fig. 6C-D and S6D-E**).

To determine whether RPIA knockdown affects cancer cells with low p16 expression *in vivo*, we injected HT-29 colon cancer cells into immunocompromised mice. Knockdown of RPIA inhibited tumor growth in HT-29 cells with shp16 but not controls (**Fig. 6E-G**). To determine whether there is increased senescence within the tumor, we looked at markers of senescence, such as decreased *LMNB1* and *CCNA2*. Consistent with our *in vitro* data, *LMNB1* was decreased only in shp16/shRPIA tumors (**Fig. 6H**). While there was a decrease in *CCNA2* upon RPIA knockdown alone, the difference was dramatically larger in shp16/shRPIA compared to shp16 alone tumors (**Fig. 6I**). Together, these data indicate that RPIA-mediated increased nucleotide synthesis is necessary for cancer cell proliferation and that suppression of RPIA may be a target for cancers with low p16 expression.

Discussion

While the role of p16 loss in deregulating the cell cycle has been known for decades (Sherr, 2001), its role in metabolism is unclear. p16 is deleted or silenced in many human cancers (Cerami et al., 2012; Gao et al., 2013); however, there is currently no approved targeted therapy for p16 low tumors (Otto and Sicinski, 2017). Therefore, identification of non-canonical downstream pathways may lead to new therapeutics for these patients. Here, we demonstrate that suppression of p16 activates mTORC1 in a non-canonical way via ATR to increase nucleotide synthesis. Mechanistically, we found mTORC1 activity led to increased translation of *RPIA* thereby increasing glucose flux through the PPP to increase nucleotide levels. Cancer cells with low p16 have increased RPIA expression and are more sensitive to inhibition of RPIA than those cells with higher p16 expression. Together, our results suggest that nucleotide metabolism via RPIA is a metabolic vulnerability of p16 low cancers.

Metabolic reprogramming is a hallmark of cancer (Hanahan and Weinberg, 2011). Cancer cells reprogram metabolism to increase biomass needed for growth and proliferation (Pavlova and Thompson, 2016). Modulation of deoxyribonucleotide levels is critical for cancer cells for proliferation and to repair DNA damage (Kohnken et al., 2015). We previously found that increased deoxyribonucleotides, either through upregulation of RRM2 expression or loss of ATM, bypasses senescence (Aird et al., 2015; Aird et al., 2013). Additionally, a recent paper found that metabolic reprogramming, including increased nucleotide levels, precedes tumor formation in a UVB-induced skin cancer

model (Hosseini et al., 2018). Here, we show for the first time that loss of p16 increases *de novo* nucleotide synthesis (**Fig. 1**). This occurred via increased expression of RPIA, an enzyme in the PPP (**Fig. 5**). Increased RPIA may be an important inflection point for metabolic reprogramming in these cells as it changes the carbon fate of glucose to support nucleotide synthesis instead of cycling back to fructose-6-phosphate (Patra and Hay, 2014). This would also maintain the generation of NADPH from the oxidative branch of the PPP.

Suppression of p16 activates mTORC1 to increase nucleotide synthesis (**Fig. 2**). mTORC1 is a master regulator of metabolism by coordinating metabolite availability to translational control of metabolic enzymes (Iurlaro et al., 2014; Zoncu et al., 2011). Recent studies have linked mTORC1 to both purine and pyrimidine synthesis via *MTHFD2* or CAD, respectively (Ben-Sahra et al., 2013; Ben-Sahra et al., 2016). However, we did not observe an increase in either pathway in our senescent bypassed cells. Instead, our results indicate that suppression of p16 increases translation of *RPIA* mRNA by mTORC1 (**Fig. 5**). Previous studies have shown in MEFs that *RPIA* is transcriptionally regulated via mTORC1-mediated signaling (Duvel et al., 2010). Our results show no change in total RPIA transcript levels (**Fig. 5B**). These previous studies were performed in *Tsc2*$^{-/-}$ MEFs, suggesting that there is a context or cell type-dependent regulation of nucleotide metabolism and RPIA by mTORC1. mTORC1 directly mediates translation of mRNAs through terminal oligopyrimidine motif (TOP) sequences, TOP-like sequences, or specific types of 5'UTRs (Gandin et al., 2016; Thoreen et al., 2012). *RPIA* has a putative TOP sequence at one of its predicted transcription start sites, suggesting the

mTORC1 may regulate *RPIA* translation via this motif. Future studies are required to determine whether this sequence is directly regulated by mTORC1 for *RPIA* translation.

ATR activation is critical in response to replication stress (Saldivar et al., 2017). Robust replication stress and the subsequent accumulation of DNA double strand breaks leads to senescence (Aird et al., 2015; Aird et al., 2013; Bartkova et al., 2006; Di Micco et al., 2006). However, low level replication stress is an early event in tumorigenesis as it can lead to genomic instability (Bester et al., 2011; Zeman and Cimprich, 2014). Interestingly, *CDKN2A* deletion or DNA methylation is also considered an early event in the development and progression of multiple cancers (Belinsky et al., 1998; Chin, 2003; Hruban et al., 2000; Nuovo et al., 1999). We found that suppression of p16 activates ATR-Chk1 signaling (**Fig. 3**), supporting the notion that these early tumorigenic events are linked. Although robust ATR activation leads to S-phase or G2 arrest (Gaillard et al., 2015; Liu et al., 2007), mild activation facilitates transformation (Lopez-Contreras et al., 2012). Consistently, ATR signaling is often critical for cancer cell survival (Karnitz and Zou, 2015; Weber and Ryan, 2015), likely due to the ability of ATR signaling to mitigate the increased replication stress that occurs in cancer cells (Zeman and Cimprich, 2014). While previous reports have linked ATR signaling to nucleotide metabolism through upregulation of RRM2 protein stability (Le et al., 2017), our model suggests that ATR also modulates nucleotide metabolism through increasing mTORC1 signaling (**Fig. 3**). Since the response to replication stress is intimately linked to nucleotide metabolism (Aird et al., 2015), it is possible that multiple redundant pathways play a role in relaying the need for nucleotides based on replication stress and DNA damage.

p16 is low in many human cancers (Cerami et al., 2012; Gao et al., 2013). We found that low p16 expression correlates with activation of ATR and mTORC1 signaling (**Fig. 4**). A previous report in a melanoma progression transgenic mouse model also found increased mTORC1 signaling upon *Cdkn2a* knockout due to miR-99/100 (Damsky et al., 2015). Our data indicate that ATR signaling regulates mTORC1 activation (**Fig. 3**), leading to nucleotide synthesis. Low p16 and activation of ATR-mTORC1 signaling occurred in multiple cell types and cancer types (**Fig. 4**), suggesting that this is a general phenomenon. Cell cycle inhibitors are currently being tested in the clinic for tumors with deletions/mutations in *CDKN2A* (clinicaltrials.gov); however, no FDA-approved therapy currently exists for this subset of patients. Excitingly, our results indicate that low p16 opens up a metabolic vulnerability through activation of mTORC1-mediated nucleotide metabolism. Indeed, we found that cells with low p16 are more sensitive to temsirolimus or suppression of RPIA both *in vitro* and *in vivo* (**Fig. 4, 6, and 7**). RPIA inhibition has been shown to limit the growth of $Kras^{G12D}$ cell lines and xenografted tumors (Santana-Codina et al., 2018; Ying et al., 2012). Our results demonstrate that RPIA expression could also be exploited as a metabolic target in cancers with low p16 expression.

In conclusion, our study provides a new molecular effect of p16 loss whereby ATR-mTORC1 signaling is activated to increase nucleotide metabolism. This is different, yet likely linked, to its canonical role in cell cycle regulation. These mechanistic insights have broad implications for understanding pro-tumorigenic metabolism. Moreover, this study

provides a new metabolic vulnerability for p16 low cancer cells, which may be exploited for therapy.

Acknowledgments

We would like to acknowledge Dr. Alice Soragni (UCLA), Dr. Kristin Eckert and Dr. Nadine Hempel (Penn State College of Medicine), Dr. Gina DeNicola (Moffitt Cancer Center), and Dr. Rugang Zhang (The Wistar Institute) for providing cell lines. We would like to thank Drs. Juan Andres Melendez and Robert P. Feehan for providing helpful discussion. This work was supported by grants from the National Institutes of Health (P50CA174523 and U54CA224070 to M.H.; DK13499 and DK15648 to S.R.K.; K22ES026235 to N.W.S.; and R00CA194309 to K.M.A.), the Dr. Miriam and Sheldon G. Adelson Medical Research Foundation (to M.H.), and the W. W. Smith Charitable Trust (to K.M.A.). The RPPA Core Facility is funded by NCI CA16672.

Author Contributions

Conceptualization, R.B. and K.M.A.; Methodology, R.K., Y.I., N.W.S.; Investigation, R.B., C.W.C, E.S.D., K.E.L., R.K., N.M., M.N., M.D., H.J., M.Z., L.K., H.L., Y.I., N.W.S., K.M.A.; Resources, G.Z., R.G., G.R., J.I.W., M.H., D.J.D.; Writing, R.B., N.W.S, and K.M.A.; Visualization, R.B., C.W.C, R.K., N.S.W., K.M.A.; Supervision, M.H., Y.L., G.B.M., G.R., J.I.W., S.R. K., D.J.D., N.W.S., K.M.A.; Funding Acquisition, G.B.M., M.H., N.W.S., and K.M.A.

Declaration of Interests

The authors declare no competing interests.

References

Aird, K.M., Worth, A.J., Snyder, N.W., Lee, J.V., Sivanand, S., Liu, Q., Blair, I.A., Wellen, K.E., and Zhang, R. (2015). ATM couples replication stress and metabolic reprogramming during cellular senescence. Cell Rep *11*, 893-901.

Aird, K.M., Zhang, G., Li, H., Tu, Z., Bitler, B.G., Garipov, A., Wu, H., Wei, Z., Wagner, S.N., Herlyn, M.*, et al.* (2013). Suppression of nucleotide metabolism underlies the establishment and maintenance of oncogene-induced senescence. Cell Rep *3*, 1252-1265.

Aird, K.M., and Zhang, R. (2014). Metabolic alterations accompanying oncogene-induced senescence. Molecular & cellular oncology *1*, e963481.

Aird, K.M., and Zhang, R. (2015). Nucleotide metabolism, oncogene-induced senescence and cancer. Cancer Lett *356*, 204-210.

Akbani, R., Ng, P.K., Werner, H.M., Shahmoradgoli, M., Zhang, F., Ju, Z., Liu, W., Yang, J.Y., Yoshihara, K., Li, J.*, et al.* (2014). A pan-cancer proteomic perspective on The Cancer Genome Atlas. Nat Commun *5*, 3887.

Bartkova, J., Rezaei, N., Liontos, M., Karakaidos, P., Kletsas, D., Issaeva, N., Vassiliou, L.V.F., Kolettas, E., Niforou, K., Zoumpourlis, V.C.*, et al.* (2006). Oncogene-induced senescence is part of the tumorigenesis barrier imposed by DNA damage checkpoints. Nature *444*, 633-637.

Belinsky, S.A., Nikula, K.J., Palmisano, W.A., Michels, R., Saccomanno, G., Gabrielson, E., Baylin, S.B., and Herman, J.G. (1998). Aberrant methylation of p16(INK4a) is an early event in lung cancer and a potential biomarker for early diagnosis. Proc Natl Acad Sci U S A *95*, 11891-11896.

Ben-Sahra, I., Howell, J.J., Asara, J.M., and Manning, B.D. (2013). Stimulation of de novo pyrimidine synthesis by growth signaling through mTOR and S6K1. Science *339*, 1323-1328.

Ben-Sahra, I., Hoxhaj, G., Ricoult, S.J.H., Asara, J.M., and Manning, B.D. (2016). mTORC1 induces purine synthesis through control of the mitochondrial tetrahydrofolate cycle. Science *351*, 728-733.

Bennecke, M., Kriegl, L., Bajbouj, M., Retzlaff, K., Robine, S., Jung, A., Arkan, M.C., Kirchner, T., and Greten, F.R. (2010). Ink4a/Arf and oncogene-induced senescence prevent tumor progression during alternative colorectal tumorigenesis. Cancer Cell *18*, 135-146.

Bennett, D.C. (2016). Genetics of melanoma progression: the rise and fall of cell senescence. Pigment cell & melanoma research *29*, 122-140.

Bester, A.C., Roniger, M., Oren, Y.S., Im, M.M., Sarni, D., Chaoat, M., Bensimon, A., Zamir, G., Shewach, D.S., and Kerem, B. (2011). Nucleotide deficiency promotes genomic instability in early stages of cancer development. Cell *145*, 435-446.

Boissan, M., Schlattner, U., and Lacombe, M.L. (2018). The NDPK/NME superfamily: state of the art. Lab Invest *98*, 164-174.

Braig, M., Lee, S., Loddenkemper, C., Rudolph, C., Peters, A.H., Schlegelberger, B., Stein, H., Dorken, B., Jenuwein, T., and Schmitt, C.A. (2005). Oncogene-induced senescence as an initial barrier in lymphoma development. Nature *436*, 660-665.

Caldwell, M.E., DeNicola, G.M., Martins, C.P., Jacobetz, M.A., Maitra, A., Hruban, R.H., and Tuveson, D.A. (2012). Cellular features of senescence during the evolution of human and murine ductal pancreatic cancer. Oncogene *31*, 1599-1608.

Cerami, E., Gao, J., Dogrusoz, U., Gross, B.E., Sumer, S.O., Aksoy, B.A., Jacobsen, A., Byrne, C.J., Heuer, M.L., Larsson, E.*, et al.* (2012). The cBio cancer genomics portal: an open platform for exploring multidimensional cancer genomics data. Cancer discovery *2*, 401-404.

Chicas, A., Wang, X., Zhang, C., McCurrach, M., Zhao, Z., Mert, O., Dickins, R.A., Narita, M., Zhang, M., and Lowe, S.W. (2010). Dissecting the unique role of the retinoblastoma tumor suppressor during cellular senescence. Cancer Cell *17*, 376-387.

Chin, L. (2003). The genetics of malignant melanoma: lessons from mouse and man. Nat Rev Cancer *3*, 559-570.

Collado, M., and Serrano, M. (2010). Senescence in tumours: evidence from mice and humans. Nat Rev Cancer *10*, 51-57.

Damsky, W., Micevic, G., Meeth, K., Muthusamy, V., Curley, D.P., Santhanakrishnan, M., Erdelyi, I., Platt, J.T., Huang, L., Theodosakis, N.*, et al.* (2015). mTORC1 activation blocks BrafV600E-induced growth arrest but is insufficient for melanoma formation. Cancer Cell *27*, 41-56.

Dankort, D., Filenova, E., Collado, M., Serrano, M., Jones, K., and McMahon, M. (2007). A new mouse model to explore the initiation, progression, and therapy of BRAFV600E-induced lung tumors. Genes Dev *21*, 379-384.

Di Micco, R., Fumagalli, M., Cicalese, A., Piccinin, S., Gasparini, P., Luise, C., Schurra, C., Garre, M., Nuciforo, P.G., Bensimon, A.*, et al.* (2006). Oncogene-induced senescence is a DNA damage response triggered by DNA hyper-replication. Nature *444*, 638-642.

Dimri, G.P., Lee, X., Basile, G., Acosta, M., Scott, G., Roskelley, C., Medrano, E.E., Linskens, M., Rubelj, I., Pereira-Smith, O.*, et al.* (1995). A biomarker that identifies senescent human cells in culture and in aging skin in vivo. Proc Natl Acad Sci U S A *92*, 9363-9367.

Dorr, J.R., Yu, Y., Milanovic, M., Beuster, G., Zasada, C., Dabritz, J.H., Lisec, J., Lenze, D., Gerhardt, A., Schleicher, K.*, et al.* (2013). Synthetic lethal metabolic targeting of cellular senescence in cancer therapy. Nature *501*, 421-425.

Duvel, K., Yecies, J.L., Menon, S., Raman, P., Lipovsky, A.I., Souza, A.L., Triantafellow, E., Ma, Q., Gorski, R., Cleaver, S.*, et al.* (2010). Activation of a metabolic gene regulatory network downstream of mTOR complex 1. Mol Cell *39*, 171-183.

Enot, D.P., Vacchelli, E., Jacquelot, N., Zitvogel, L., and Kroemer, G. (2018). TumGrowth: An open-access web tool for the statistical analysis of tumor growth curves. Oncoimmunology *7*, e1462431.

Finch, R.A., Liu, M., Grill, S.P., Rose, W.C., Loomis, R., Vasquez, K.M., Cheng, Y., and Sartorelli, A.C. (2000). Triapine (3-aminopyridine-2-carboxaldehyde-thiosemicarbazone): A potent inhibitor of ribonucleotide reductase activity with broad spectrum antitumor activity. Biochem Pharmacol *59*, 983-991.

Finch, R.A., Liu, M.C., Cory, A.H., Cory, J.G., and Sartorelli, A.C. (1999). Triapine (3-aminopyridine-2-carboxaldehyde thiosemicarbazone; 3-AP): an inhibitor of ribonucleotide reductase with antineoplastic activity. Adv Enzyme Regul *39*, 3-12.

Gaillard, H., Garcia-Muse, T., and Aguilera, A. (2015). Replication stress and cancer. Nat Rev Cancer *15*, 276-289.

Gandin, V., Masvidal, L., Hulea, L., Gravel, S.P., Cargnello, M., McLaughlan, S., Cai, Y., Balanathan, P., Morita, M., Rajakumar, A.*, et al.* (2016). nanoCAGE reveals 5' UTR features that define specific modes of translation of functionally related MTOR-sensitive mRNAs. Genome Res *26*, 636-648.

Gao, J., Aksoy, B.A., Dogrusoz, U., Dresdner, G., Gross, B., Sumer, S.O., Sun, Y., Jacobsen, A., Sinha, R., Larsson, E.*, et al.* (2013). Integrative analysis of complex cancer genomics and clinical profiles using the cBioPortal. Science signaling *6*, pl1.

Goel, V.K., Ibrahim, N., Jiang, G., Singhal, M., Fee, S., Flotte, T., Westmoreland, S., Haluska, F.S., Hinds, P.W., and Haluska, F.G. (2009). Melanocytic nevus-like hyperplasia and melanoma in transgenic BRAFV600E mice. Oncogene *28*, 2289-2298.

Guo, L., Worth, A.J., Mesaros, C., Snyder, N.W., Glickson, J.D., and Blair, I.A. (2016). Diisopropylethylamine/hexafluoroisopropanol-mediated ion-pairing ultra-high-performance liquid chromatography/mass spectrometry for phosphate and carboxylate metabolite analysis: utility for studying cellular metabolism. Rapid Commun Mass Spectrom *30*, 1835-1845.

Haferkamp, S., Becker, T.M., Scurr, L.L., Kefford, R.F., and Rizos, H. (2008). p16INK4a-induced senescence is disabled by melanoma-associated mutations. Aging Cell *7*, 733-745.

Hakansson, P., Hofer, A., and Thelander, L. (2006). Regulation of mammalian ribonucleotide reduction and dNTP pools after DNA damage and in resting cells. J Biol Chem *281*, 7834-7841.

Hanahan, D., and Weinberg, R.A. (2011). Hallmarks of Cancer: The Next Generation. Cell *144*, 646-674.

Herman, J.G., Merlo, A., Mao, L., Lapidus, R.G., Issa, J.P., Davidson, N.E., Sidransky, D., and Baylin, S.B. (1995). Inactivation of the CDKN2/p16/MTS1 gene is frequently associated with aberrant DNA methylation in all common human cancers. Cancer Res *55*, 4525-4530.

Hernandez-Segura, A., Nehme, J., and Demaria, M. (2018). Hallmarks of Cellular Senescence. Trends Cell Biol *28*, 436-453.

Hilton, B.A., Li, Z., Musich, P.R., Wang, H., Cartwright, B.M., Serrano, M., Zhou, X.Z., Lu, K.P., and Zou, Y. (2016). ATR Plays a Direct Antiapoptotic Role at Mitochondria, which Is Regulated by Prolyl Isomerase Pin1. Mol Cell *61*, 487.

Hosseini, M., Dousset, L., Mahfouf, W., Serrano-Sanchez, M., Redonnet-Vernhet, I., Mesli, S., Kasraian, Z., Obre, E., Bonneu, M., Claverol, S.*, et al.* (2018). Energy Metabolism Rewiring Precedes UVB-Induced Primary Skin Tumor Formation. Cell Rep *23*, 3621-3634.

Hruban, R.H., Goggins, M., Parsons, J., and Kern, S.E. (2000). Progression model for pancreatic cancer. Clin Cancer Res *6*, 2969-2972.

Iurlaro, R., Leon-Annicchiarico, C.L., and Munoz-Pinedo, C. (2014). Regulation of cancer metabolism by oncogenes and tumor suppressors. Methods Enzymol *542*, 59-80.

Kabbarah, O., Nogueira, C., Feng, B., Nazarian, R.M., Bosenberg, M., Wu, M., Scott, K.L., Kwong, L.N., Xiao, Y., Cordon-Cardo, C.*, et al.* (2010). Integrative genome comparison of primary and metastatic melanomas. PLoS One *5*, e10770.

Karnitz, L.M., and Zou, L. (2015). Molecular Pathways: Targeting ATR in Cancer Therapy. Clin Cancer Res *21*, 4780-4785.

Kohnken, R., Kodigepalli, K.M., and Wu, L. (2015). Regulation of deoxynucleotide metabolism in cancer: novel mechanisms and therapeutic implications. Mol Cancer *14*, 176.

Kriegl, L., Neumann, J., Vieth, M., Greten, F.R., Reu, S., Jung, A., and Kirchner, T. (2011). Up and downregulation of p16(Ink4a) expression in BRAF-mutated polyps/adenomas indicates a senescence barrier in the serrated route to colon cancer. Mod Pathol *24*, 1015-1022.

Kuskovsky, R., Buj, R., Xu, P., Hofbauer, S., Doan, M.T., Jiang, H., Bostwick, A., Mesaros, C., Aird, K.M., and Snyder, N.W. (2018). Simultaneous isotope dilution

quantification and metabolic tracing of deoxyribonucleotides by liquid chromatography high resolution mass spectrometry. bioRxiv.

Lane, A.N., and Fan, T.W.M. (2015). Regulation of mammalian nucleotide metabolism and biosynthesis. In Nucleic Acids Research, pp. 2466-2485.

Le, T.M., Poddar, S., Capri, J.R., Abt, E.R., Kim, W., Wei, L., Uong, N.T., Cheng, C.M., Braas, D., Nikanjam, M.*, et al.* (2017). ATR inhibition facilitates targeting of leukemia dependence on convergent nucleotide biosynthetic pathways. Nat Commun *8*, 241.

Lecona, E., and Fernandez-Capetillo, O. (2014). Replication stress and cancer: it takes two to tango. Exp Cell Res *329*, 26-34.

Lee, D.F., Kuo, H.P., Chen, C.T., Hsu, J.M., Chou, C.K., Wei, Y., Sun, H.L., Li, L.Y., Ping, B., Huang, W.C.*, et al.* (2007). IKK beta suppression of TSC1 links inflammation and tumor angiogenesis via the mTOR pathway. Cell *130*, 440-455.

Li, J., Poi, M.J., and Tsai, M.D. (2011). Regulatory mechanisms of tumor suppressor P16(INK4A) and their relevance to cancer. Biochemistry *50*, 5566-5582.

Li, Z., Kong, Y., Song, L., Luo, Q., Liu, J., Shao, C., Hou, X., and Liu, X. (2018). Plk1-Mediated Phosphorylation of TSC1 Enhances the Efficacy of Rapamycin. Cancer Res *78*, 2864-2875.

Liu, E., Lee, A.Y., Chiba, T., Olson, E., Sun, P., and Wu, X. (2007). The ATR-mediated S phase checkpoint prevents rereplication in mammalian cells when licensing control is disrupted. J Cell Biol *179*, 643-657.

Lopez-Contreras, A.J., Gutierrez-Martinez, P., Specks, J., Rodrigo-Perez, S., and Fernandez-Capetillo, O. (2012). An extra allele of Chk1 limits oncogene-induced replicative stress and promotes transformation. J Exp Med *209*, 455-461.

Lynch, C.J., Kimball, S.R., Xu, Y., Salzberg, A.C., and Kawasawa, Y.I. (2015). Global deletion of BCATm increases expression of skeletal muscle genes associated with protein turnover. Physiol Genomics *47*, 569-580.

Ma, X.M., and Blenis, J. (2009). Molecular mechanisms of mTOR-mediated translational control. Nat Rev Mol Cell Biol *10*, 307-318.

Ma, Y., Vassetzky, Y., and Dokudovskaya, S. (2018). mTORC1 pathway in DNA damage response. Biochim Biophys Acta.

Magnuson, B., Ekim, B., and Fingar, D.C. (2012). Regulation and function of ribosomal protein S6 kinase (S6K) within mTOR signalling networks. Biochem J *441*, 1-21.

Mannava, S., Moparthy, K.C., Wheeler, L.J., Natarajan, V., Zucker, S.N., Fink, E.E., Im, M., Flanagan, S., Burhans, W.C., Zeitouni, N.C.*, et al.* (2013). Depletion of

deoxyribonucleotide pools is an endogenous source of DNA damage in cells undergoing oncogene-induced senescence. Am J Pathol *182*, 142-151.

Matsuoka, S., Ballif, B.A., Smogorzewska, A., McDonald, E.R., 3rd, Hurov, K.E., Luo, J., Bakalarski, C.E., Zhao, Z., Solimini, N., Lerenthal, Y*., et al.* (2007). ATM and ATR substrate analysis reveals extensive protein networks responsive to DNA damage. Science *316*, 1160-1166.

Merlo, A., Herman, J.G., Mao, L., Lee, D.J., Gabrielson, E., Burger, P.C., Baylin, S.B., and Sidransky, D. (1995). 5' CpG island methylation is associated with transcriptional silencing of the tumour suppressor p16/CDKN2/MTS1 in human cancers. Nat Med *1*, 686-692.

Michaloglou, C., Vredeveld, L.C., Soengas, M.S., Denoyelle, C., Kuilman, T., van der Horst, C.M., Majoor, D.M., Shay, J.W., Mooi, W.J., and Peeper, D.S. (2005). BRAFE600-associated senescence-like cell cycle arrest of human naevi. Nature *436*, 720-724.

Nandagopal, N., and Roux, P.P. (2015). Regulation of global and specific mRNA translation by the mTOR signaling pathway. Translation (Austin, Tex) *3*, e983402.

Nordlund, P., and Reichard, P. (2006). Ribonucleotide Reductases. Annual Review of Biochemistry *75*, 681-706.

Nuovo, G.J., Plaia, T.W., Belinsky, S.A., Baylin, S.B., and Herman, J.G. (1999). In situ detection of the hypermethylation-induced inactivation of the p16 gene as an early event in oncogenesis. Proc Natl Acad Sci U S A *96*, 12754-12759.

Ortega, S., Malumbres, M., and Barbacid, M. (2002). Cyclin D-dependent kinases, INK4 inhibitors and cancer. Biochim Biophys Acta *1602*, 73-87.

Otto, T., and Sicinski, P. (2017). Cell cycle proteins as promising targets in cancer therapy. Nat Rev Cancer *17*, 93-115.

Patra, K.C., and Hay, N. (2014). The pentose phosphate pathway and cancer. Trends Biochem Sci *39*, 347-354.

Pavlova, N.N., and Thompson, C.B. (2016). The Emerging Hallmarks of Cancer Metabolism. Cell Metab *23*, 27-47.

Perez-Mancera, P.A., Young, A.R., and Narita, M. (2014). Inside and out: the activities of senescence in cancer. Nat Rev Cancer *14*, 547-558.

Postigo, A., Ramsden, A.E., Howell, M., and Way, M. (2017). Cytoplasmic ATR Activation Promotes Vaccinia Virus Genome Replication. Cell Rep *19*, 1022-1032.

Saldivar, J.C., Cortez, D., and Cimprich, K.A. (2017). The essential kinase ATR: ensuring faithful duplication of a challenging genome. Nat Rev Mol Cell Biol *18*, 622-636.

Santana-Codina, N., Roeth, A.A., Zhang, Y., Yang, A., Mashadova, O., Asara, J.M., Wang, X., Bronson, R.T., Lyssiotis, C.A., Ying, H.*, et al.* (2018). Oncogenic KRAS supports pancreatic cancer through regulation of nucleotide synthesis. Nat Commun *9*, 4945.

Sarkisian, C.J., Keister, B.A., Stairs, D.B., Boxer, R.B., Moody, S.E., and Chodosh, L.A. (2007). Dose-dependent oncogene-induced senescence in vivo and its evasion during mammary tumorigenesis. Nat Cell Biol *9*, 493-505.

Serrano, M., Lin, A.W., McCurrach, M.E., Beach, D., and Lowe, S.W. (1997). Oncogenic ras provokes premature cell senescence associated with accumulation of p53 and p16INK4a. Cell *88*, 593-602.

Shain, A.H., Joseph, N.M., Yu, R., Benhamida, J., Liu, S., Prow, T., Ruben, B., North, J., Pincus, L., Yeh, I.*, et al.* (2018). Genomic and Transcriptomic Analysis Reveals Incremental Disruption of Key Signaling Pathways during Melanoma Evolution. Cancer Cell *34*, 45-55.e44.

Shain, A.H., Yeh, I., Kovalyshyn, I., Sriharan, A., Talevich, E., Gagnon, A., Dummer, R., North, J., Pincus, L., Ruben, B.*, et al.* (2015). The Genetic Evolution of Melanoma from Precursor Lesions. N Engl J Med *373*, 1926-1936.

Sherr, C.J. (2001). The INK4a/ARF network in tumour suppression. Nat Rev Mol Cell Biol *2*, 731-737.

Shima, K., Nosho, K., Baba, Y., Cantor, M., Meyerhardt, J.A., Giovannucci, E.L., Fuchs, C.S., and Ogino, S. (2011). Prognostic significance of CDKN2A (p16) promoter methylation and loss of expression in 902 colorectal cancers: Cohort study and literature review. Int J Cancer *128*, 1080-1094.

Talantov, D., Mazumder, A., Yu, J.X., Briggs, T., Jiang, Y., Backus, J., Atkins, D., and Wang, Y. (2005). Novel genes associated with malignant melanoma but not benign melanocytic lesions. Clin Cancer Res *11*, 7234-7242.

Thoreen, C.C., Chantranupong, L., Keys, H.R., Wang, T., Gray, N.S., and Sabatini, D.M. (2012). A unifying model for mTORC1-mediated regulation of mRNA translation. Nature *485*, 109-113.

Trefely, S., Ashwell, P., and Snyder, N.W. (2016). FluxFix: automatic isotopologue normalization for metabolic tracer analysis. BMC Bioinformatics *17*, 485.

Uphoff, C.C., and Drexler, H.G. (2005). Detection of mycoplasma contaminations. Methods Mol Biol *290*, 13-23.

Weber, A.M., and Ryan, A.J. (2015). ATM and ATR as therapeutic targets in cancer. Pharmacol Ther *149*, 124-138.

Wiley, C.D., and Campisi, J. (2016). From Ancient Pathways to Aging Cells-Connecting Metabolism and Cellular Senescence. Cell Metab *23*, 1013-1021.

Yaswen, P., and Campisi, J. (2007). Oncogene-induced senescence pathways weave an intricate tapestry. Cell *128*, 233-234.

Ying, H., Kimmelman, A.C., Lyssiotis, C.A., Hua, S., Chu, G.C., Fletcher-Sananikone, E., Locasale, J.W., Son, J., Zhang, H., Coloff, J.L.*, et al.* (2012). Oncogenic Kras maintains pancreatic tumors through regulation of anabolic glucose metabolism. Cell *149*, 656-670.

Zeman, M.K., and Cimprich, K.A. (2014). Causes and consequences of replication stress. In Nature Cell Biology, pp. 2-9.

Zhang, Q., Wang, J., Deng, F., Yan, Z., Xia, Y., Wang, Z., Ye, J., Deng, Y., Zhang, Z., Qiao, M.*, et al.* (2015). TqPCR: A Touchdown qPCR Assay with Significantly Improved Detection Sensitivity and Amplification Efficiency of SYBR Green qPCR. PLoS One *10*, e0132666.

Zhou, X., Liu, W., Hu, X., Dorrance, A., Garzon, R., Houghton, P.J., and Shen, C. (2017). Regulation of CHK1 by mTOR contributes to the evasion of DNA damage barrier of cancer cells. Scientific reports *7*, 1535.

Zoncu, R., Efeyan, A., and Sabatini, D.M. (2011). mTOR: from growth signal integration to cancer, diabetes and ageing. Nat Rev Mol Cell Biol *12*, 21-35.

Figures and Figure Legends

Figure 1- Buj et al.

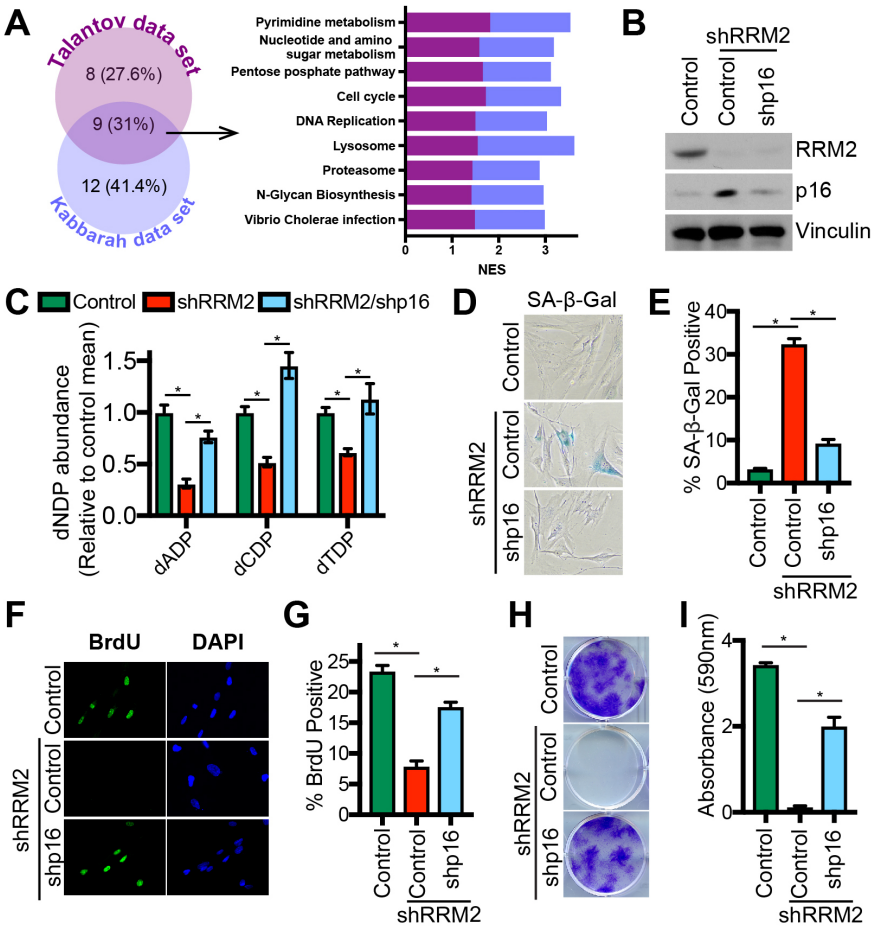

Figure 1. Suppression of p16 increases nucleotide synthesis to bypass senescence.

(A) KEGG Pathway analysis of two publicly-available datasets comparing benign nevi with melanoma. NES (Normalized Enriched Score).

(B-I) Normal diploid IMR90 cells were infected with lentivirus expressing short hairpin RNAs (shRNAs) targeting RRM2 (shRRM2) alone or in combination with an shRNA targeting p16 (shp16). Empty vector was used as a control.

(B) Immunoblot analysis of RRM2 and p16. Vinculin was used as a loading control. One of 5 experiments is shown.

(C) dNDP analysis was performed by LC-HRMS. n>3/group, one of 2 experiments is shown. Data represent mean ± SEM. *p<0.05

(D) SA-β-Gal activity. One of 5 experiments is shown.

(E) Quantification of (D). n=3/group, one of 5 experiments is shown. Data represent mean ± SD. *p<0.01

(F) BrdU incorporation. One of 5 experiments is shown.
(G) Quantification of (F). n=3/group, one of 5 experiments is shown. Data represent mean ± SEM. *p<0.01
(H) Colony formation. Cells were seeded at an equal density and 14 days later stained with 0.05% crystal violet. One of 5 experiments is shown.
(I) Quantification of (G). Crystal violet plates were destained, and the absorbance was read at 590nm. n=3/group, one of 5 experiments is shown. Data represent mean ± SEM. *p<0.001

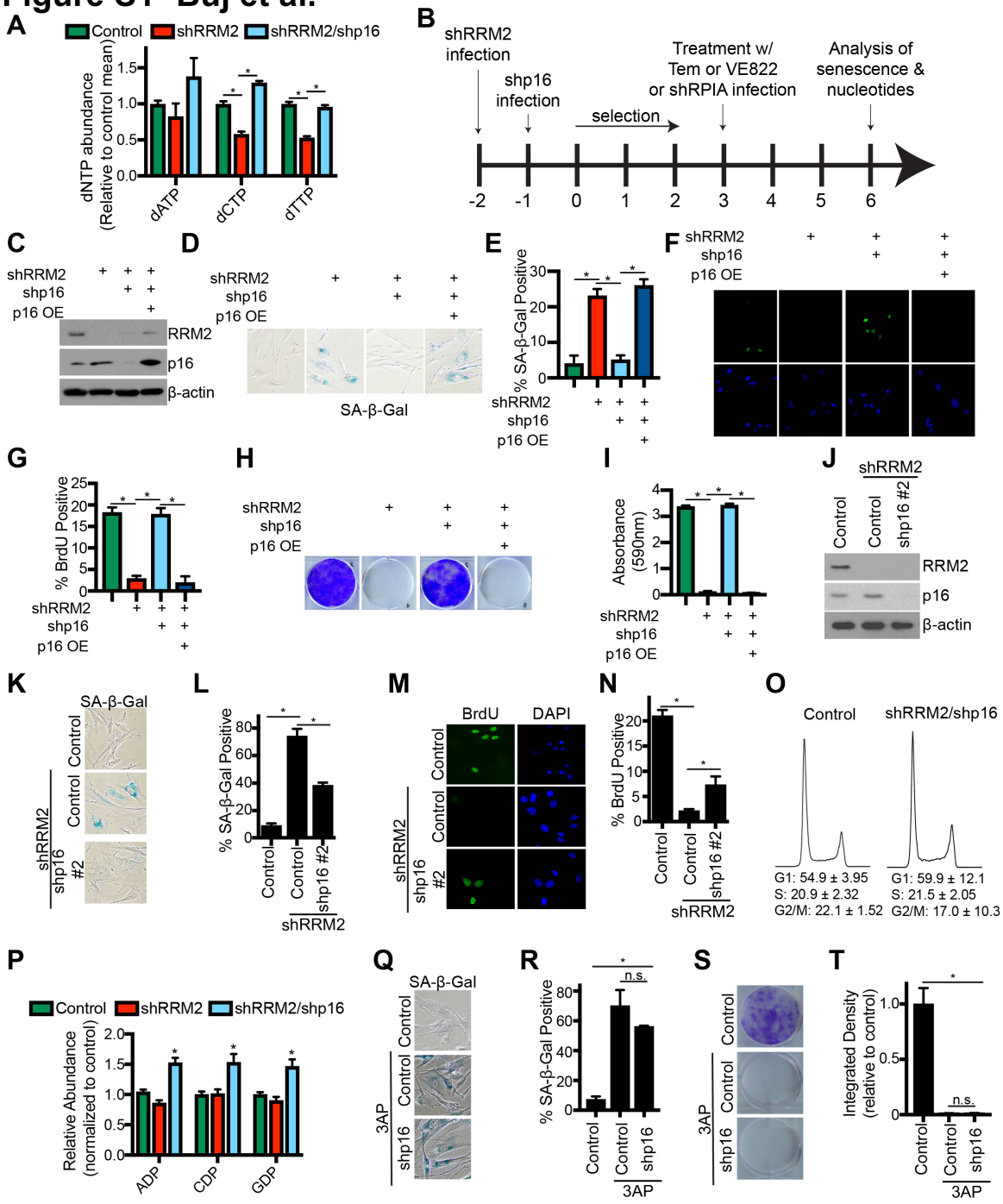

Figure S1. Suppression of p16 increases dNTP synthesis through the *de novo* pathway; related to Figure 1.

(A) Normal diploid IMR90 cells were infected with lentivirus expressing short hairpin RNAs (shRNAs) targeting RRM2 (shRRM2) alone or in combination with an shRNA targeting p16 (shp16). Empty vector was used as a control. dNTPs were quantified using

LC-HRMS. n>2/group, one of 2 experiments is shown. Data represent mean ± SD. *p<0.05

(B) Schematic of infection and treatment of cells.

(C-I) Same as (A), but cells were also infected with a retrovirus expressing *CDKN2A* cDNA.

(C) Immunoblot analysis of RRM2 and p16. β-actin was used as a loading control. One of 2 experiments is shown.

(D) SA-β-Gal activity. One of 2 experiments is shown.

(E) Quantification of (D). n=3/group, one of 2 experiments is shown. Data represent mean ± SEM. *p<0.0005

(F) BrdU incorporation. One of 2 experiments is shown.

(G) Quantification of (F). n=3/group, one of 2 experiments is shown. Data represent mean ± SEM. *p<0.01

(H) Colony formation. One of 2 experiments is shown.

(I) Quantification of (H). n=3/group, one of 2 experiments is shown. Data represent mean ± SEM. *p<0.0001

(J-N) Same as (B), but a second, independent shRNA targeting p16 was used.

(J) Immunoblot analysis of RRM2 and p16. β-actin was used as a loading control. One of 3 experiments is shown.

(K) SA-β-Gal activity. One of 3 experiments is shown.

(L) Quantification of (K). n=3/group, one of 3 experiments is shown. Data represent mean ± SEM. *p<0.001

(M) BrdU incorporation. One of 3 experiments is shown.

(N) Quantification of (M). n=3/group, one of 3 experiments is shown. Data represent mean ± SEM. *p<0.05

(O) Same as (B) but cell cycle was determined by PI staining in the indicated cells.

(P) NDP quantification by LC-HRMS. n>9/group. Data represent mean ± SEM of 2 experiments. *p<0.005 vs. control and shRRM2

(Q-T) Normal diploid IMR90 cells were infected with lentivirus expressing shRNA targeting p16 (shp16) alone or in combination with (10μM) 3AP. Empty vector was used as a control. Cells were treated for 7 days.

(Q) SA-β-Gal activity. One of 2 experiments is shown.

(R) Quantification of (Q). n=3/group, one of 2 experiments is shown. Data represent mean ± SEM. *p<0.005, n.s.= not significant

(S) Colony formation. Cells were seeded at an equal density and 14 days later stained with 0.05% crystal violet. One of 2 experiments is shown.

(T) Quantification of (S). Crystal violet plates were destained, and the absorbance was read at 590nm. n=3/group, one of 2 experiments is shown. Data represent mean ± SEM. *p<0.005, n.s.= not significant

Figure 2- Buj et al.

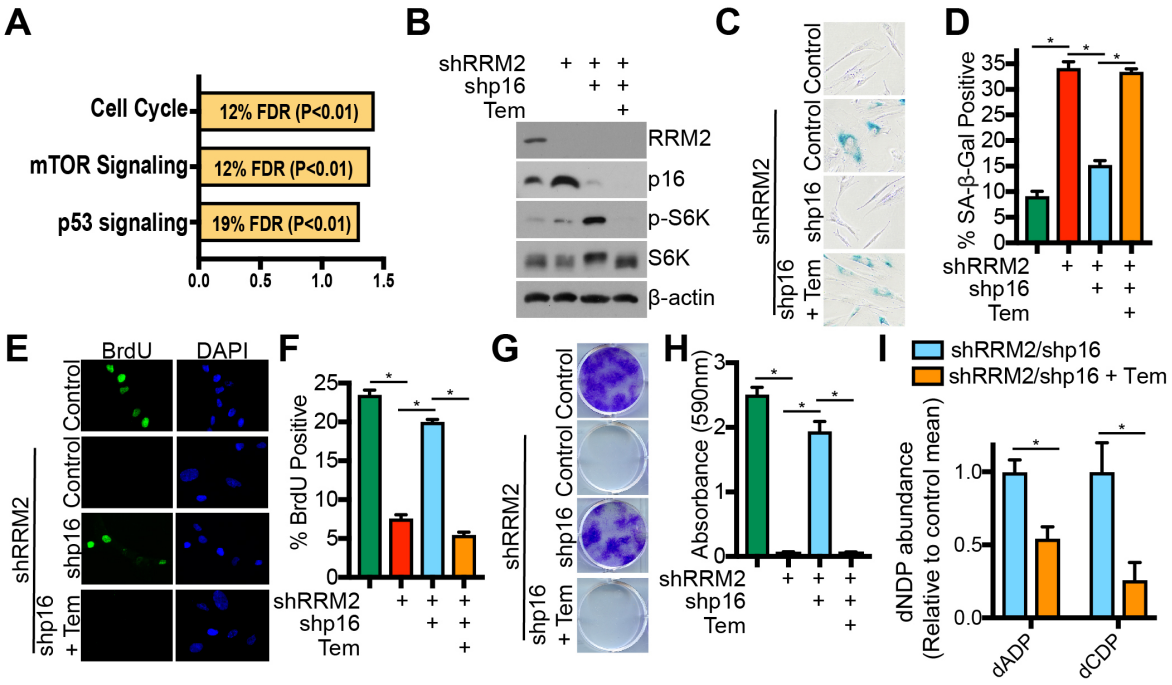

Figure 2. Suppression of p16 activates mTORC1 increase nucleotide synthesis.
(A-B) Normal diploid IMR90 cells were infected with lentivirus expressing short hairpin RNA (shRNAs) targeting RRM2 (shRRM2) alone or in combination with an shRNA targeting p16 (shp16). Empty vector was used as a control. **(B-J)** Temsirolimus (0.5nM) was added 4 days after starting selection.
(A) KEGG Pathway analysis of reverse phase protein array (RPPA) data.
(B) Immunoblot analysis of RRM2, p16, p-S6K (Thr389), and total S6K. β-actin was used as a loading control. One of 3 experiments is shown.
(C) SA-β-Gal activity. One of 3 experiments is shown.
(D) Quantification of (C). n=3/group, one of 3 experiments is shown. Data represent mean ± SEM. *p<0.01
(E) BrdU incorporation. One of 3 experiments is shown.
(F) Quantification of (E). n=3/group, one of 3 experiments is shown. Data represent mean ± SEM. *p<0.05
(G) Colony formation. Cells were seeded at an equal density and 14 days later stained with 0.05% crystal violet. One of 3 experiments is shown.
(H) Quantification of (G). Crystal violet plates were destained, and the absorbance was read at 590nm. n=3/group, one of 3 experiments is shown. Data represent mean ± SEM. *p<0.01
(I) Quantification of dADP and dCDP by LC-HRMS. n=3/group, one of 2 experiments is shown. Data represent mean ± SEM. *p<0.05

Figure S2- Buj et al.

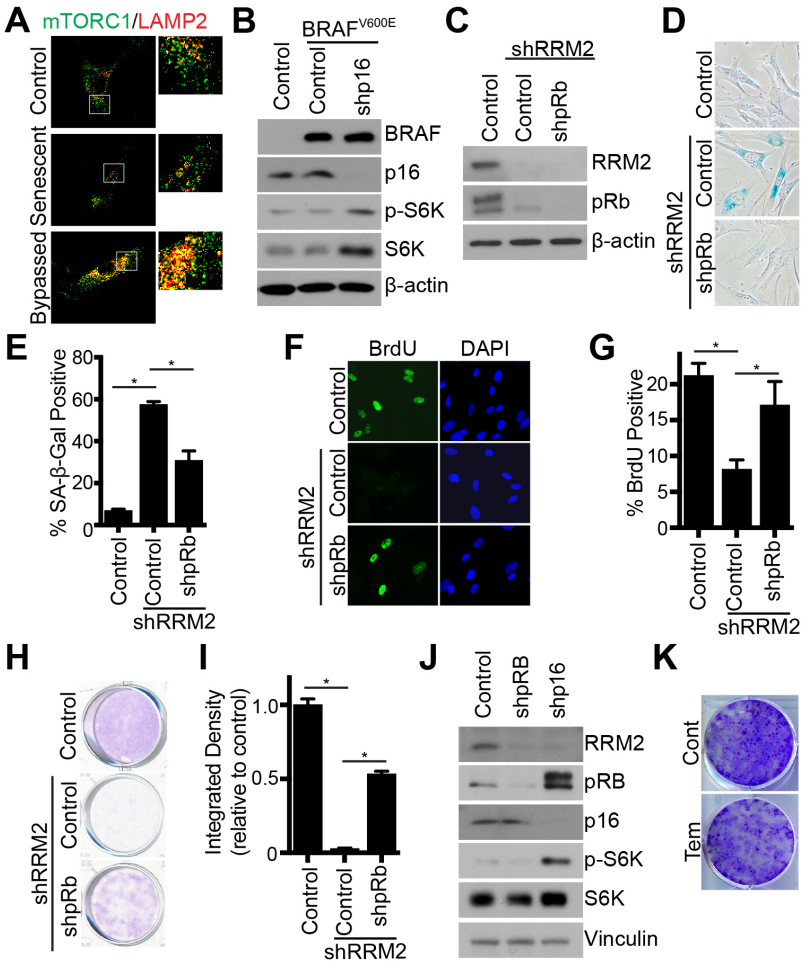

Figure S2. Suppression of p16 activates mTORC1 in a BRAF^{V600E} model of senescence bypass; suppression of pRb does not activate mTORC1 to bypass senescence; related to Figure 2.

(A) Normal diploid IMR90 cells were infected with lentivirus expressing short hairpin RNA (shRNAs) targeting RRM2 (shRRM2) alone or in combination with an shRNA targeting p16 (shp16). Empty vector was used as a control. Confocal microscopy images of co-localization of immunofluorescence staining using anti-mTORC1 and anti-LAMP2 antibodies.

(B) Normal diploid IMR90 cells were infected with retrovirus expressing BRAF^{V600E} alone or in combination with a lentivirus expressing shRNA targeting p16 (shp16). Empty vector was used as a control. Immunoblot analysis of BRAF, p16, p-S6K (Thr389), and total S6K. β-actin was used as a loading control. One of 2 experiments is shown.

(C-I) Normal diploid IMR90 cells were infected with lentivirus expressing short hairpin RNA (shRNAs) targeting RRM2 (shRRM2) alone or in combination with an shRNA targeting pRb (shpRb). Empty vector was used as a control. Cells were selected with puromycin for 7 days.

(C) Immunoblot analysis of RRM2 and pRb. β-actin was used as a loading control. One of 4 experiments is shown.
(D) SA-β-Gal activity. One of 4 experiments is shown.
(E) Quantification of (D). n=3/group, one of 4 experiments is shown. Data represent mean ± SEM. *p<0.01
(F) BrdU incorporation. One of 4 experiments is shown.
(G) Quantification of (F). n=3/group, one of 3 experiments is shown. Data represent mean ± SEM. *p<0.05
(H) Colony formation. Cells were seeded at an equal density and 14 days later stained with 0.05% crystal violet. One of 4 experiments is shown.
(I) Quantification of (H). Integrated density of wells was determined using ImageJ. n=3/group, one of 4 experiments is shown. Data represent mean ± SEM. *$p<10^{-4}$
(J) Normal diploid IMR90 cells were infected with lentivirus expressing short shRNAs targeting RRM2 in combination with shRNA targeting p16 (shp16) or pRb (shpRb). Empty vector was used as a control. Cells were selected with puromycin for 7 days. Immunoblot analysis of RRM2, pRb, p16, p-S6K (Thr389), and total S6K. Vinculin was used as a loading control. One of 2 experiments is shown.
(K) Normal diploid IMR90 cells were treated with 0.5nM temsirolimus for 3 days and stained with 0.05% crystal violet.

Figure 3- Buj et al.

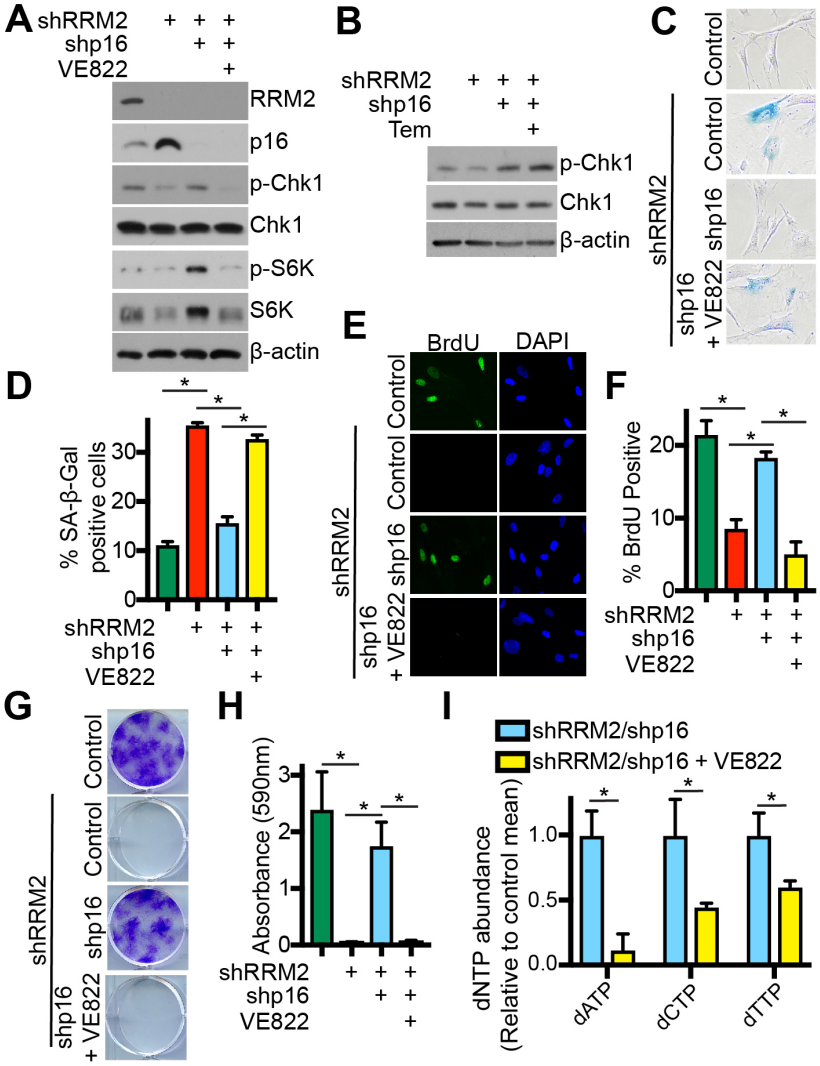

Figure 3. Suppression of p16 activates ATR signaling to increase mTORC1 and nucleotide synthesis.

(A-I) Normal diploid IMR90 cells were infected with lentivirus expressing short hairpin RNA (shRNAs) targeting RRM2 (shRRM2) alone or in combination with an shRNA targeting p16 (shp16). Empty vector was used as a control. **(A-J)** VE822 (10nM) or Temsirolimus (0.5nM) was added 4 days after starting selection.

(A) Immunoblot analysis of RRM2, p16, p-Chk1 (Ser345), total Chk1, p-S6K (Thr389), and total S6K. β-actin was used as a loading control. One of 3 experiments is shown.

(B) Immunoblot analysis of p-Chk1 (Ser345) and total Chk1. β-actin was used as a loading control. One of 3 experiments is shown.

(C) SA-β-Gal activity. One of 3 experiments is shown.

(D) Quantification of (C). n=3/group, one of 3 experiments is shown. Data represent mean ± SD. *p<0.01

(E) BrdU incorporation. One of 3 experiments is shown.

(F) Quantification of (E). n=3/group, one of 3 experiments is shown. Data represent mean ± SD. *p<0.001
(G) Colony formation. Cells were seeded at an equal density and 14 days later stained with 0.05% crystal violet. One of 3 experiments is shown.
(H) Quantification of (G). Crystal violet plates were destained, and the absorbance was read at 590nm. n=3/group, one of 3 experiments is shown. Data represent mean ± SD. *p<0.01
(I) dNTP analysis was performed by LC-HRMS. n>4/group. Data represent mean ± SEM of 2 experiments. *p<0.005

Figure S3- Buj et al.

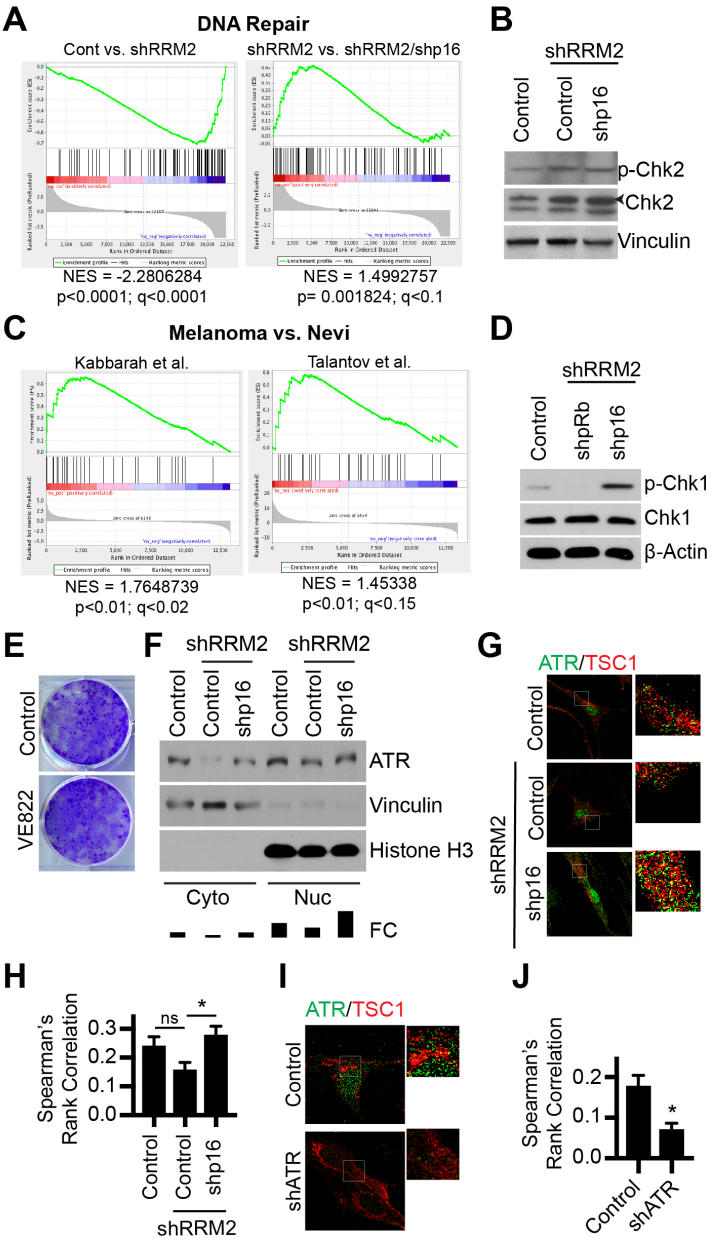

Figure S3. Suppression of p16 does not activate Chk2; ATR is cytoplasmic and co-localizes with TSC1; related to Figure 3.

(A-B) Normal diploid IMR90 cells were infected with lentivirus expressing short hairpin RNA (shRNAs) targeting RRM2 (shRRM2) alone or in combination with an shRNA targeting p16 (shp16). Empty vector was used as a control.

(A) DNA Repair GSEA Reactome enrichment analysis in control vs. shRRM2 and shRRM2 vs. shRRM2/shp16 cells.

(B) Immunoblot analysis of p-Chk2 (Thr68) and total Chk2. Vinculin was used as a loading control.

(C) DNA Repair GSEA Reactome enrichment analysis in melanoma vs. nevi samples using publicly-available data (Kabbarah et al., 2010; Talantov et al., 2005).
(D) Same as (A) but shRRM2 cells were infected with a lentivirus expressing an shRNA targeting pRb. Immunoblot analysis of p-Chk1 (Ser345) and total Chk1. β-actin was used as a loading control.
(E) Normal diploid IMR90 cells were treated with 10nM VE822 for 3 days and stained with 0.05% crystal violet.
(F) Same as (A), but cytoplasmic and nuclear fractions were harvested. Immunoblot analysis of ATR. Vinculin was used as a loading control. Histone H3 was used to show purity of the cytoplasmic fraction. ATR fold change (FC) was performed using ImageJ.
(G) Same as (A), but ATR and TSC1 immunofluorescence was performed. Shown are confocal images.
(H) Co-localization analysis using Coloc 2 plugin for ImageJ. Shown is Spearman's Rank Correlation. n=>6/group, one of 2 experiments are shown. Data represent mean ± SEM. ns = not significant; *p<0.02
(I) IMR90 cells were infected with a lentivirus expression a short hairpin RNA to ATR. ATR and TSC1 immunofluorescence was performed. Shown are confocal images.
(J) Co-localization analysis using Coloc 2 plugin for ImageJ. Shown is Spearman's Rank Correlation. n=2/group, one of 2 experiments are shown. Data represent mean ± SEM. *p<0.05

Figure 4- Buj et al.

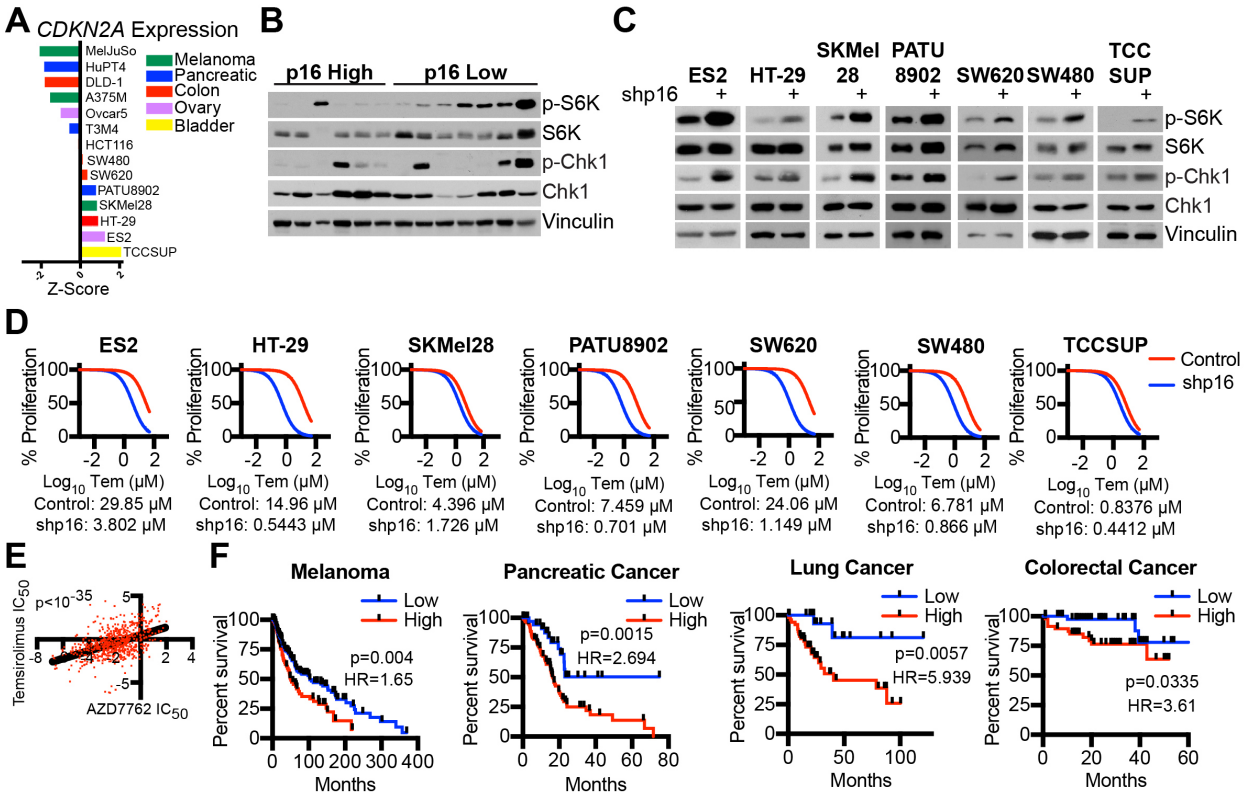

Figure 4. ATR-mTORC1 signaling axis is activated in p16 low cancers and is a therapeutic vulnerability for cancer cells with low p16.

(A) Analysis of *CDKN2A* expression using TCGA data. Shown are Z-scores.

(B) Immunoblot analysis of p16, p-S6K (Thr389), total S6K, p-Chk1 (Ser345), and total Chk1 in p16 high and p16 low cell lines. Vinculin was used as a loading control. Loading (left to right): ES2, HT-29, SKMel28, PATU8902, SW620, SW480, HCT116, T3M4, Ovcar5, A375M, DLD-1, HuPT4, MelJuSo.

(C) The indicated cancer cell lines with high p16 expression were infected with a short hairpin targeting p16. Cells were serum starved for 16h after which they were incubated with 10% FBS for 30 min. Immunoblot analysis of p16, p-S6K (Thr389), total S6K, p-Chk1 (Ser345). One of at least 2 experiments is shown.

(D) The indicated cancer cell lines with high p16 expression were infected with a short hairpin targeting p16 and then treated with a dose-course of temsirolimus under 0.5% FBS conditions. n=3/group, one of 2 experiments is shown. Data represent non-linear fit of transformed data. IC_{50} for each condition is indicated.

(E) Temsirolimus IC_{50} correlates with AZD7762 (Chk1 inhibitor) IC_{50}. Data from the Dependency Map (depmap.org). $p<10^{-35}$

(F) Kaplan Meier curves of overall survival for melanoma, pancreatic, or lung cancer patients with high or low expression of leading-edge genes in “Translation” and “DNA Repair” GSEA terms from RNA-Seq analysis (Table S4). Melanoma patients shown have mutant BRAF or NRAS; pancreatic and lung cancer patients shown have mutant KRAS; colorectal adenocarcinoma cancer patients shown have mutant KRAS, BRAF, or NRAS. mRNA expression z-score threshold = 4.5, 2, 2, and 3 respectively.

Figure S4- Buj et al.

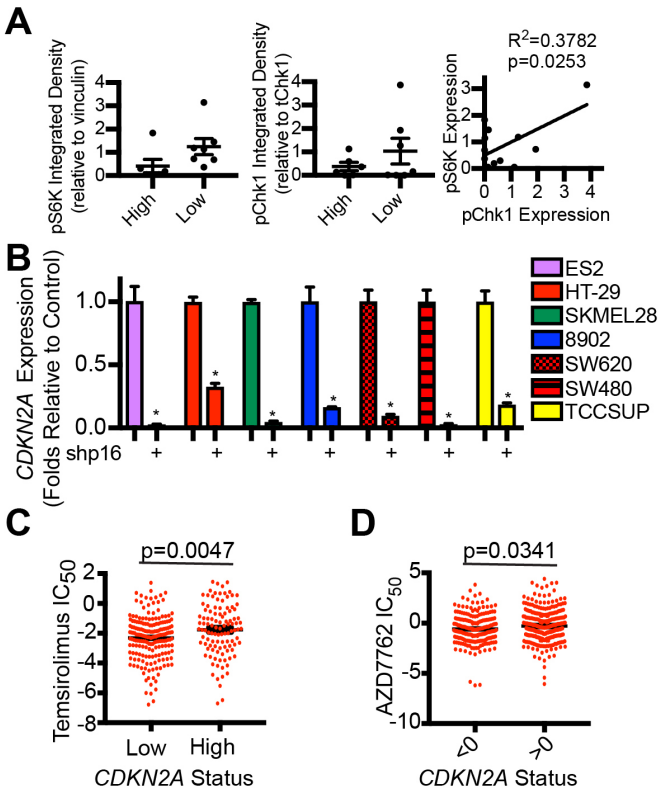

Figure S4. p16 expression status of cancer cell lines correlates with temsirolimus and AZD7762 sensitivity; related to Figure 4.

(A) Integrated density analysis of pS6K compared to vinculin (left) and pChk1 compared to total Chk1 (middle) from western blots shown in Fig. 4B. Correlation analysis between pS6K and pChk1 is shown on the right. Data represent mean ± SEM. One of 2 experiments is shown.

(B) The indicated cancer cells were infected with a lentivirus expressing p16 shRNA, and *CDKN2A* expression was determined by qRT-PCR. Data represent mean ± SD. *p<0.01

(C) Analysis of *CDKN2A* copy number and temsirolimus IC_{50} data from the Dependency Map (depmap.org).

(D) Analysis of *CDKN2A* expression and AZD7762 IC_{50} data from the Dependency Map (depmap.org).

Figure 5- Buj et al.

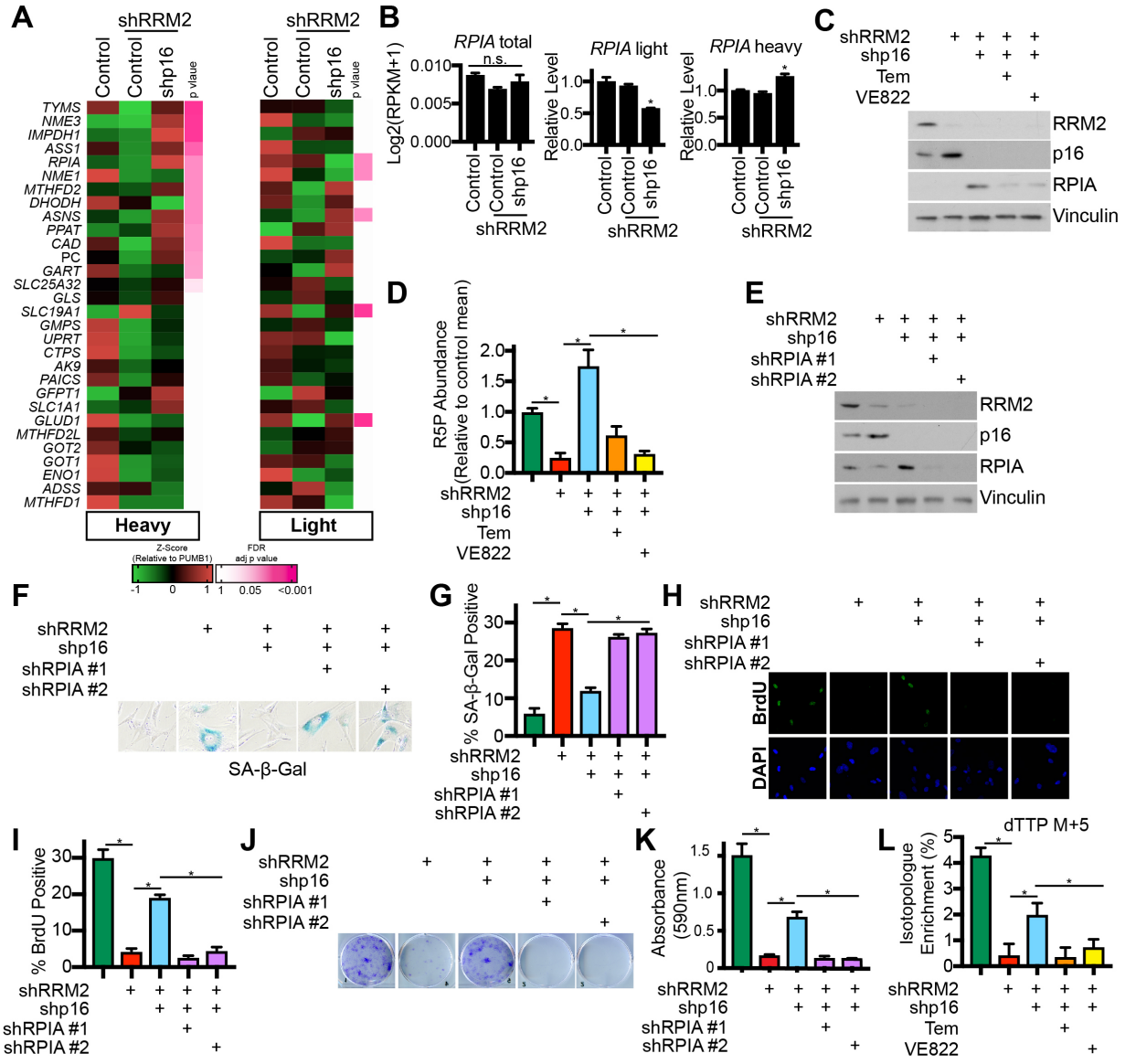

Figure 5. Suppression of p16 increases RPIA translation via mTORC1 to increase nucleotide synthesis.

(A-D) Normal diploid IMR90 cells were infected with lentivirus expressing short hairpin RNA (shRNAs) targeting RRM2 (shRRM2) alone or in combination with an shRNA targeting p16 (shp16). Empty vector was used as a control. Cells were selected with puromycin for 7 days. **(C-D)** Temsirolimus (0.5nM) or VE822 (10nM) was added 4 days after starting selection.

(A) Heatmap of light and heavy fractions from polysome profiling.

(B) *RPIA* expression in total (left), light (middle), and heavy (right) fractions. n=3/group. Data represent mean ± SEM. *p<0.005

(C) Immunoblot analysis of RRM2, p16, and RPIA. Vinculin was used as a loading control. One of 3 experiments is shown.

(D) Ribose-5-phosphate levels were determined by LC-HRMS. n>3/group. Data represent mean ± SEM. *p<0.01
(E-L) shRRM2/shp16 cells were infected with lentivirus expressing 2 independent hairpins targeting RPIA.
(E) Immunoblot analysis of RRM2, p16, and RPIA. Vinculin used as a loading control. One of 3 experiments is shown.
(F) SA-β-Gal activity. One of 3 experiments is shown.
(G) Quantification of (F). n=3/group, one of 3 experiments is shown. Data represent mean ± SEM. *p<0.05
(H) BrdU incorporation. One of 3 experiments is shown.
(I) Quantification of (H). n=3/group, one of 3 experiments is shown. Data represent mean ± SEM. *p<0.001
(J) Colony formation. Cells were seeded at an equal density and 14 days later stained with 0.05% crystal violet. One of 3 experiments is shown.
(K) Quantification of (J). Crystal violet plates were destained, and the absorbance was read at 590nm. n=3/group, one of 3 experiments is shown. Data represent mean ± SEM. *p<0.05
(L) Cells were incubated with U-^{13}C glucose for 8 hours. dTTP M+5 was detected by LC-HRMS. n>3/group. Data represent mean ± SEM. *p<0.05

Figure S5- Buj et al.

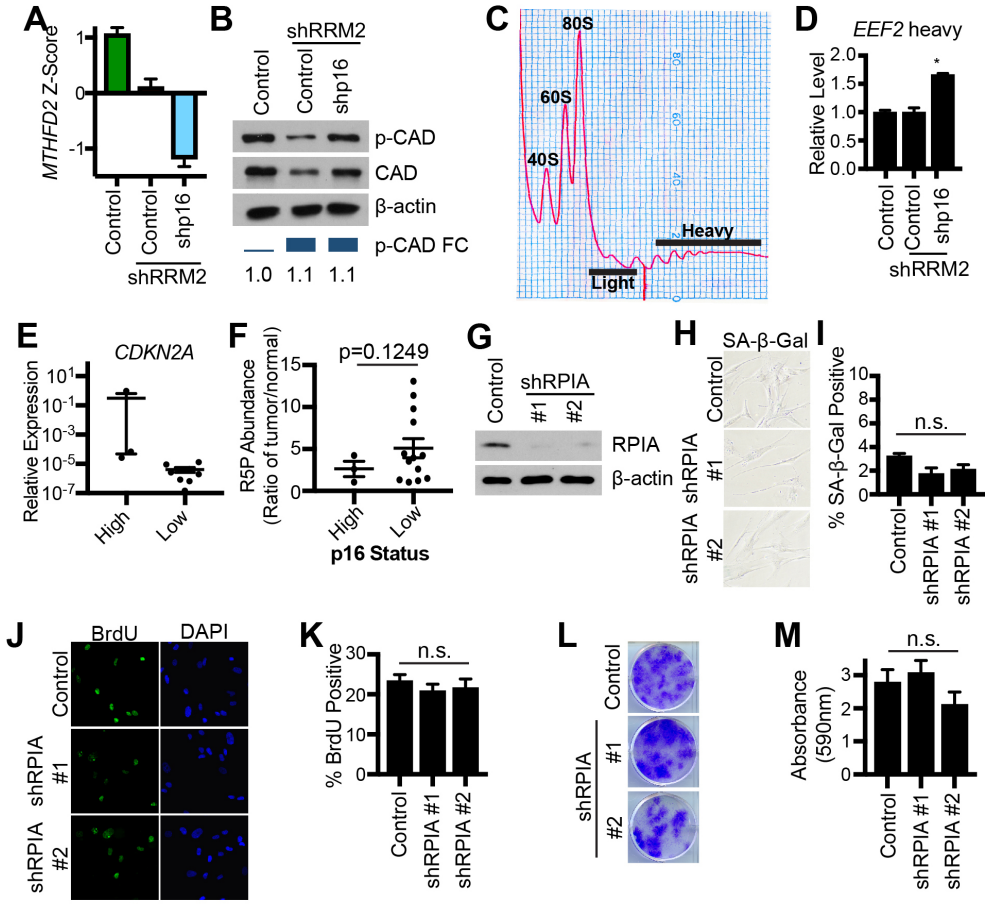

Figure S5. Suppression of p16 does not affect *MTHFD2* or CAD; knockdown of RPIA does not affect control IMR90; related to Figure 5.

(A-D) Normal diploid IMR90 cells were infected with lentivirus expressing short hairpin RNA (shRNAs) targeting RRM2 (shRRM2) alone or in combination with an shRNA targeting p16 (shp16). Empty vector was used as a control.

(A) *MTHFD2* expression from RNA-Seq analysis. n=3/group. Data represent mean ± SEM.

(B) Immunoblot analysis of p-CAD (Ser1859) and total CAD. β-actin was used as a loading control. p-CAD fold change (FC) was performed relative to β-actin using ImageJ.

(C) Representative polysome profile. "Light" and "Heavy" fractions are indicated.

(D) *EEF2* expression in heavy fraction. n=3/group. Data represent mean ± SD. *p<0.001

(E-F) Melanoma and pancreatic cancer patient specimens.

(E) qRT-PCR analysis of *CDKN2A*.

(F) Ribose-5-phosphate abundance as a ratio of tumor compared to paired normal tissue.

(G-M) Normal diploid IMR90 cells were infected with lentivirus expressing two independent short hairpin RNA (shRNAs) targeting RPIA (shRPIA #1 and #2). Empty vector was used as a control.

(G) Immunoblot analysis of RPIA. β-actin was used as a loading control.

(H) SA-β-Gal activity. One of 3 experiments is shown.
(I) Quantification of (H). n=3/group, one of 3 experiments is shown. Data represent mean ± SEM. n.s.= not significant
(J) BrdU incorporation. One of 3 experiments is shown.
(K) Quantification of (J). n=3/group, one of 3 experiments is shown. Data represent mean ± SEM. n.s.= not significant
(L) Colony formation. Cells were seeded at an equal density and 14 days later stained with 0.05% crystal violet. One of 3 experiments is shown.
(M) Quantification of (L). Crystal violet plates were destained, and the absorbance was read at 590nm. n=3/group, one of 3 experiments is shown. Data represent mean ± SEM. n.s.= not significant

Figure 6- Buj et al.

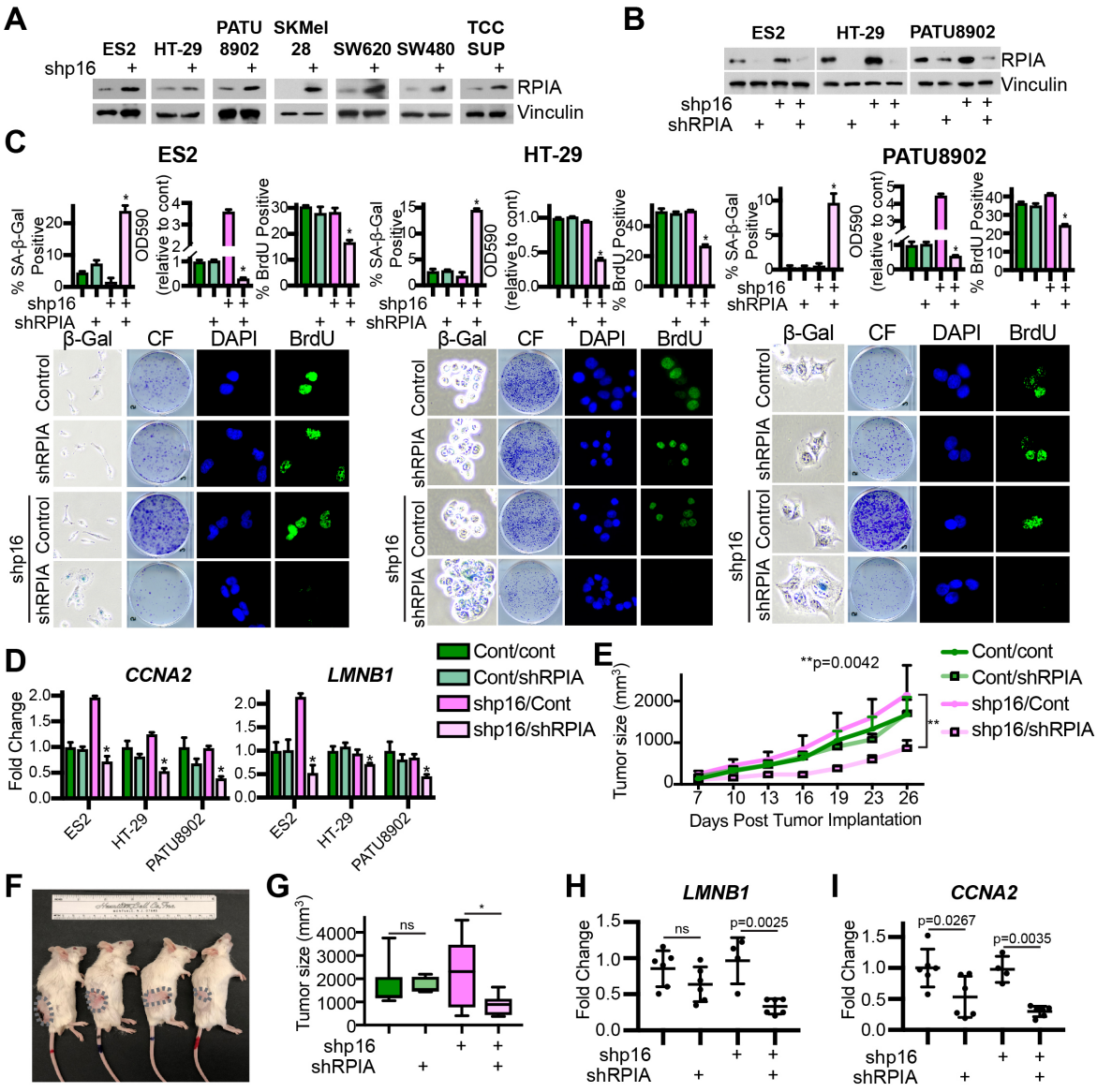

Figure 6. Inhibition of RPIA is a metabolic vulnerability for cancer cells with low p16.

(A) The indicated cancer cell lines with high p16 expression were infected with a short hairpin targeting p16. Cells were serum starved for 16h after which they were incubated with 10% FBS for 30 min. Immunoblot analysis of RPIA. Vinculin was used as a loading control. One of at least 2 experiments is shown.

(B-D) The indicated cancer cell lines with high p16 expression were infected with a short hairpin targeting RPIA alone or in combination with a shRNA targeting p16.

(B) RPIA western blot analysis of the indicated cell lines. Vinculin was used as a loading control. One of at least 2 experiments is shown.

(C) SA-β-Gal activity, colony formation (CF), and BrdU incorporation for each of the indicated cell lines. n=3/group, one of at least 2 experiments is shown. Data represent mean ± SEM. *p<0.05 vs. shp16 alone.
(D) *CCNA2* and *LMNB1* fold change in the indicated cells. One of at least 2 experiments is shown. Data represent mean ± SD. *p<0.05 vs. shp16 alone.
(E) HT-29 colon cancer cells expressing control or p16 shRNA alone or in combination with RPIA shRNA were injected into the flank of SCID mice (4-6 mice/group). Shown is the tumor growth curve over 26 days.
(F) Representative images of mice from each group. Tumors are outlined in gray.
(G) Tumor volume at Day 26 post-implantation. *p=0.0414; ns= not significant
(H) *LMNB1* fold change in the indicated tumors. ns= not significant
(I) *CCNA2* fold change in the indicated tumors.

Figure S6- Buj et al.

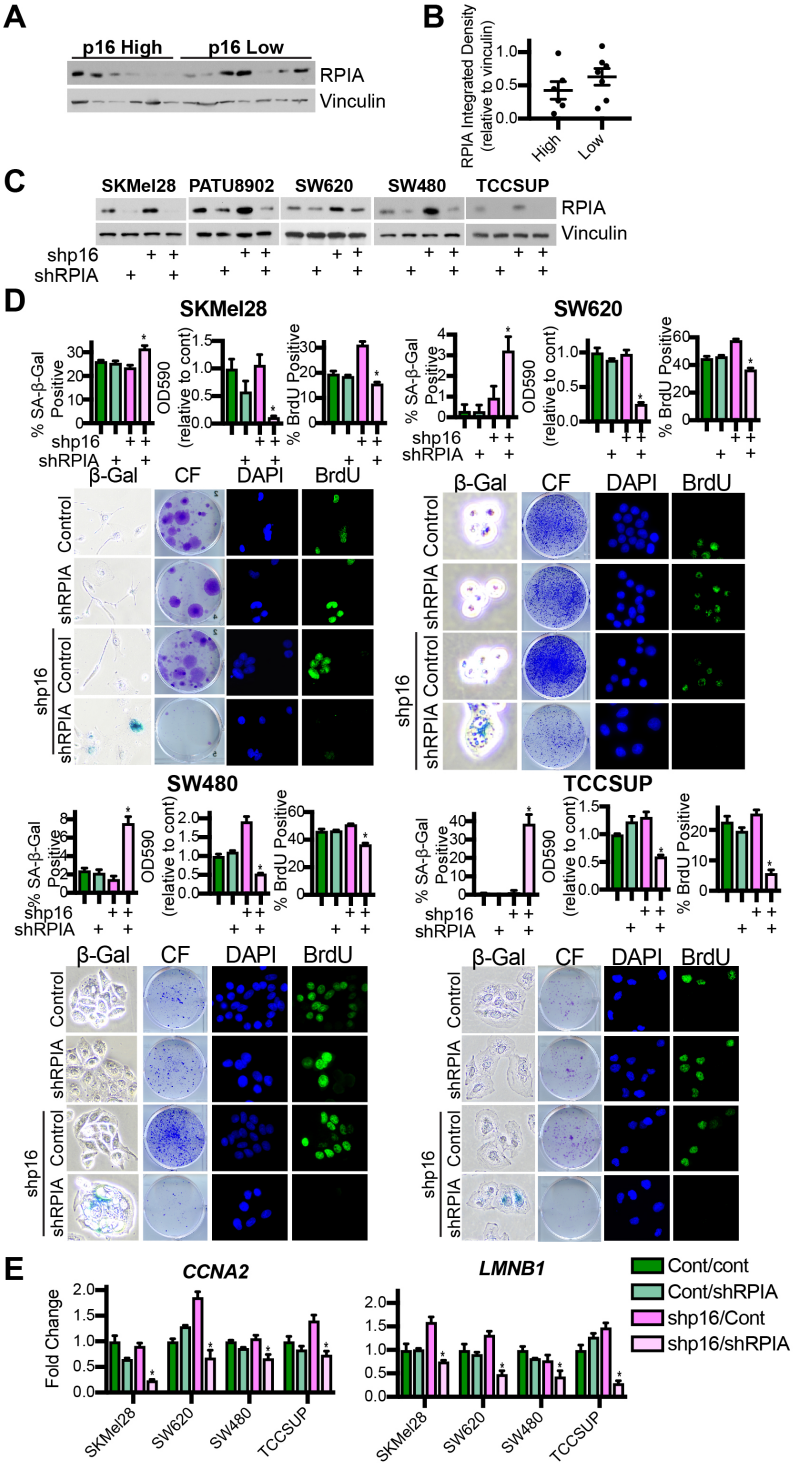

Figure S6. RPIA protein expression correlates with p16 expression; related to Figure 6.

(A) Immunoblot analysis of RPIA in p16 high and p16 low cell lines. Vinculin was used as a loading control. Loading (left to right): ES2, HT-29, SKMel28, PATU8902, SW620,

SW480, HCT116, T3M4, Ovcar5, A375M, DLD-1, HuPT4, MelJuSo. One of 2 experiments is shown.

(B) Integrated density analysis of RPIA compared to vinculin. Data represent mean ± SEM. One of 2 experiments is shown.

(C-E) The indicated cancer cell lines with high p16 expression were infected with a short hairpin targeting RPIA alone or in combination with a shRNA targeting p16.

(C) RPIA western blot analysis of the indicated cell lines. Vinculin was used as a loading control. One of at least 2 experiments is shown.

(D) SA-β-Gal activity, colony formation (CF), and BrdU incorporation for each of the indicated cell lines. n=3/group, one of at least 2 experiments is shown. Data represent mean ± SEM. *p<0.05 vs. shp16 alone.

(E) *CCNA2* and *LMNB1* fold change in the indicated cells. One of at least 2 experiments is shown. Data represent mean ± SD. *p<0.05 vs. shp16 alone.

STAR Methods

Contact for Reagent and Resource Sharing

Further information and requests for resources and reagents should be directed to and will be fulfilled by the Lead Contact, Katherine M. Aird (kaird@psu.edu).

REAGENT or RESOURCE	SOURCE	IDENTIFIER
Experimental Models: Human derived Cell Lines		
Fibroblasts: IMR90	R. Zhang Laboratory	ATCC CCL-186
Fibroblasts: IMR90 shControl	This paper	N/A
Fibroblasts: IMR90 shRRM2	This paper	N/A
Fibroblasts: IMR90 shp16	This paper	N/A
Fibroblasts: IMR90 shRRM2/shp16	This paper	N/A
Fibroblasts: IMR90 shRRM2/shpRb	This paper	N/A
Fibroblasts: IMR90 shRPIA	This paper	N/A
Fibroblasts: IMR90 shRRM2/shp16/shRPIA	This paper	N/A
Embryonic kidney: 293FT	R. Zhang Laboratory	Thermo Fisher R70007
Embryonic kidney: Phoenix (QNX)	Dr. Gary Nolan	N/A
Skin: A375	G. Robertson Laboratory	ATCC CRL-1619
Skin: MelJuSo	G. Robertson Laboratory	N/A
Skin: SKMel28	G. Robertson Laboratory	ATCC HTB-72
Skin: SKMel28 shControl	This paper	N/A
Skin: SKMel28 shRPIA	This paper	N/A
Skin: SKMel28shp16	This paper	N/A
Skin: SKMel28shp16/shRPIA	This paper	N/A
Pancreas: HuPT4	A. Soragni Laboratory	
Pancreas: T3M4	G. DeNicola Laboratory	N/A
Pancreas: PATU8902	G. DeNicola Laboratory	N/A
Pancreas: PATU8902 shControl	This paper	N/A
Pancreas: PATU8902 shRPIA	This paper	N/A

Pancreas: PATU8902 shp16	This paper	N/A
Pancreas: PATU8902 shp16/shRPIA	This paper	N/A
Ovary: OVCAR5	R. Zhang Laboratory	N/A
Ovary: ES-2	N. Hempel Laboratory	ATCC crl-1978
Ovary: ES-2 shControl	This paper	N/A
Ovary: ES-2 shRPIA		
Ovary: ES-2 shp16	This paper	N/A
Ovary: ES-2 shp16/shRPIA	This paper	N/A
Bladder: TCC-SUB	D. Degraff Laboratory	ATCC HTB-5
Bladder: TCC-SUB shControl	This paper	N/A
Bladder: TCC-SUB shRPIA	This paper	N/A
Bladder: TCC-SUB shp16	This paper	N/A
Bladder: TCC-SUB shp16/shRPIA	This paper	N/A
Colon: DLD-1	K. Eckert Laboratory	ATCC CCL-221
Colon: HCT116	K. Eckert Laboratory	ATCC CCL-247
Colon: SW620	K. Eckert Laboratory	ATCC CCL-227
Colon: SW620 shControl	This paper	N/A
Colon: SW620 shRPIA	This paper	N/A
Colon: SW620 shp16	This paper	N/A
Colon: SW620 shp16/shRPIA	This paper	N/A
Colon: SW480	K. Eckert Laboratory	ATCC CCL-228
Colon: SW480 shControl	This paper	N/A
Colon: SW480 shRPIA	This paper	N/A
Colon: SW480 shp16	This paper	N/A
Colon: SW480 shp16/shRPIA	This paper	N/A
Colon: HT-29	K. Eckert Laboratory	ATCC HTB-38
Colon: HT-29 shControl	This paper	N/A
Colon: HT-29 shRPIA	This paper	N/A
Colon: HT-29 shp16	This paper	N/A
Colon: HT-29 shp16/shRPIA	This paper	N/A
Antibodies		
RRM2 (WB)	Santa Cruz Biotechnology	Cat # sc-398294
p16 (WB, IHC)	Abcam	Cat# ab108349, RRID:AB_10858268
Vinculin	Sigma-Aldrich	Cat# V9131, RRID:AB_477629
S6K (WB)	Cell Signaling Technology	Cat# 2708, RRID:AB_390722
Phospho S6K (Thr389) (WB)	Cell Signaling Technology	Cat# 9234, RRID:AB_2269803
Phospho S6K (Th389) (IHC)		

β-Actin	Sigma-Aldrich	Cat# A1978, RRID:AB_476692
Chk1	Cell Signaling Technology	Cat# 2360S, RRID:AB_10694643
Phospho Chk1 (Ser345)	Cell Signaling Technology	Cat# 2348, RRID:AB_331212
RPIA	Abcam	Cat# ab181235
BRAF	Santa Cruz Biotechnology	Cat# sc-5284, RRID:AB_2721130
pRb	BD Biosciences	Cat# 554136, RRID:AB_39525
Chk2	Cell Signaling Technology	Cat# 2662, RRID:AB_2080793
Phospho Chk2 (Thr68)	Cell Signaling Technology	Cat# 2661, RRID:AB_331479
CAD	Cell Signaling Technology	Cat# 11933
Phospho CAD (Ser1859)	Cell Signaling Technology	Cat # 70307
BrdU	Abcam	Cat# ab6326, RRID:AB_305426
mTORC1	Cell Signaling Technology	Cat# 2983, RRID:AB_2105622
LAMP2	Santa Cruz Biotechnology	Cat# sc-18822, RRID:AB_626858
TSC1	Thermo Fisher Scientific	Cat# 37-0400, RRID:AB_2533292
Anti-mouse HRP	Cell Signaling Technology	Cat# 7076, RRID:AB_330924
Anti-rabbit HRP	Cell Signaling Technology	Cat# 7074, RRID:AB_2099233
Anti-rat FITCI	Jackson ImmunoResearch Labs	Cat# 712-095-150, RRID:AB_2340651
Anti-rabbit FITCI	Jackson ImmunoResearch Labs	Cat# 711-095-152, RRID:AB_2315776
Anti-mouse Cy3	Jackson ImmunoResearch Labs	Cat# 715-165-150, RRID:AB_2340813
Bacterial strains		
Stbl3™ Chemically Competent E.	Fisher Scientific	Cat# C737303
DH5α™ Competent Cells	Fisher Scientific	Cat# 18265-017
Virus		
pLKO.1 Control lentiviral vector	Addgene	Cat #8453

pLKO.1 shRRM2 lentiviral vector	Sigma-Aldrich	TRCN0000049410
pLKO.1 shp16 #1 lentiviral vector	Sigma-Aldrich	TRCN0000010482
pLKO.1 shp16 #2 lentiviral vector	Sigma-Aldrich	TRCN0000039751
pLKO.1 shpRb lentiviral vector	Sigma-Aldrich	
pLKO.1 shRPIA #1 lentiviral vector	Sigma-Aldrich	TRCN0000049410
pLKO.1 shRPIA #2 lentiviral vector	Sigma-Aldrich	TRCN0000049411
pLKO.1 shATR #1 lentiviral vector	Sigma-Aldrich	TCRN0000039615
pLKO.1 shATR #2 lentiviral vector	Sigma-Aldrich	TCRN0000039616
pBABE control retroviral vector	Addgene	Cat #1764
pBABE p16 OE retroviral vector	R. Zhang Laboratory	N/A
pBABE BRAFV600E retroviral vector	Addgene	Cat #15269
Chemicals, Peptides, and Recombinant Proteins		
BrdU	Alfa Aesar	Cat #H27260
X-Gal	Sigma-Aldrich	Cat# B4252
D-Glucose-13C6	Sigma-Aldrich	Cat# 389374
Puromycin	Gibco	Cat# A11138-02
Polybrene	Sigma-Aldrich	Cat# H9268
Propidium Iodide	Sigma-Aldrich	P4170
Crystal violet	Harleco	Cat# 192-12
Software		
GSEA	Broad Institute	N/A
GraphPad Prism 7	N/A	N/A
IDT tool for primer design	Integrated DNA Technologies	N/A
Cufflinks	Version v.2.0.2	N/A
Others		
DMEM 17	Corning	Cat# 10-017-CV
DMEM 13	Corning	Cat# 10-013-CV
RPMI	Gibco	Cat# 11875093
DMEM w/o glucose or glutamine	Sigma-Aldrich	Cat# D5030
MEM/EBSS glutamine	HyClone	Cat# SH30024.01
MEM Nonessential Amino Acids	Corning	Cat# 25025CL
Glutagro	Corning	Cat# 25015CL

Sodium Bicarbonate	Corning	Cat# 25035CL
Sodium Pyruvate	Corning	Cat# 25000CL
FBS	VWR	Cat# 16000-044
Charcoal stripped FBS	Sigma-Aldrich	Cat# F6765
Lipofectamine 2000	Invitrogen	Cat# 11668019
Trizol	Ambion	Cat# 15596018
Glutaraldehyde	Polysciences, Inc.	Cat# 01909
RNAse Out	Invitrogen	Cat# 10777019
Formaldehyde	VWR	Cat# 0493
Paraformaldehyde	Sigma-Aldrich	Cat# 158127
VE822	Selleckchem	Cat# S7102
Temsirolimus	Selleckchem	Cat# S1044
3AP	Sigma-Aldrich	Cat# SML0568

Experimental Model and Subject Details

Cell Lines

Normal diploid IMR90 human fibroblasts were cultured according to the ATCC in low oxygen (2% O_2) in DMEM (4.5 g/L glucose, corning cat#10017CV) with 10% FBS supplemented with L-glutamine, non-essential amino acids, sodium pyruvate, and sodium bicarbonate. Experiments were performed on IMR90 between population doubling #25-35. Melanoma (SKMel28, A375, and MelJuSo), pancreatic (HuPT4, T3M4, and PATU8902), colorectal (DLD-1, HT-29, SW620, SW480, and HCT116) tumor cells and lentiviral and retroviral packaging cells (293FT and Phoenix, respectively) were cultured in DMEM (corning, cat#10013CV) with 10% FBS. Ovary tumor cell lines (ES2 and OVCAR5) were cultured in RPMI medium 1640 with 10% FBS. TCCSUP bladder cancer cells were cultured in MEM/EBSS glutamine supplemented with 10% FBS. All cell lines were cultured in MycoZap and were routinely tested for mycoplasma as described in (Uphoff and Drexler, 2005). All cell lines were authenticated using STR Profiling using Genetica DNA Laboratories.

Patient Samples

Frozen melanoma and pancreatic cancer tissue along with adjacent normal tissue were obtained from the Penn State Institute for Personalized Medicine (IPM), Hershey, PA. All experiments were performed in accordance with institutional guidelines approved by the Institutional Review Board (IRB) at the Penn State College of Medicine.

Mice

Two-month old male SCID mice were purchased from Charles River Laboratories. All mice were maintained in a HEPA-filtered ventilated rack system at the Milton S. Hershey Medical Center animal facility. Mice were housed up to 4 mice per cage and in a 12-hour light/dark cycle. All experiments with animals were performed in accordance with institutional guidelines approved by the Institutional Animal Care and Use Committee (IACUC) at the Penn State College of Medicine.

Method details

Lentiviral and retroviral packaging and infection

Retrovirus production and transduction were performed using the BBS/calcium chloride method (Aird et al., 2013). Phoenix cells (a gift from Dr. Gary Nolan, Stanford University) were used to package the infection viruses. Lentiviral constructs were transfected into 293FT cells using Lipofectamine 2000 (Thermo Fisher). Lentivirus was packaged using the ViraPower Kit (Invitrogen, Carlsbad, CA, USA) following the manufacturer's instructions.

The basic IMR90 experiment timeline is delineated in **Figure S1B**. Briefly, IMR90 cells were infected with pLKO.1 empty vector or pLKO.1-shRRM2, and 24 hours later cells were infected with pLKO.1 empty vector or pLKO.1-shp16 to generate control (pLKO.1/pLKO.1), senescence (pLKO.1-shRRM2/pLKO.1) and senescence bypass (pLKO.1-shRRM2/pLKO.1-shp16). Cells were selected with puromycin (3μg/mL) for 7 days. Where indicated, cells were treated at day 4 with Temsirolimus (0.5nM) or VE822 (10nM) or infected with pLKO.1-shRPIA. p16 rescue experiment was performed by simultaneous infection with pLKO.1-shp16 and pBABE-p16 overexpression plasmid. For single infections, cells were infected with the corresponding virus and selected in puromycin (1μg/mL) for 7 days.

Tumor cell lines were infected with pLKO.1 or pLKO.1-shp16. Cells were selected with puromycin (1μg/mL) for 4 days. Where indicated, cells were treated at day 4 with increasing concentrations of Temsirolimus (0.07-50nM) or infected with shRPIA. For double infections, cells were infected with the corresponding virus and selected in puromycin (3μg/mL) for 4 additional days.

RNA-Sequencing and Analysis

Total RNA was extracted from cells with Trizol (Life Technologies) and DNAse treated with RNeasy Mini Kit (Qiagen, cat#74104) following the manufacturer's instructions. RNA integrity number (RIN) was measured using BioAnalyzer (Agilent Technologies) RNA 6000 Nano Kit to confirm RIN above 7. The cDNA libraries were prepared using KAPA Stranded RNA-Seq Kits with RiboErase (Kapa Biosystems). Next generation sequencing

was performed in The Penn State College of Medicine Genome Sciences and Bioinformatics Core facility as previously described in (Lynch et al., 2015) using a HiSeq 2500 sequencer (Illumina). Demultiplexed and quality-filtered mRNA-Seq reads were then aligned to human reference genome (GRCh38) using TopHat (v.2.0.9). Differential expression analysis was done using Cuffdiff tool which is available by Cufflinks (v.2.0.2) as described in (Lynch et al., 2015).

Reverse Phase Protein Array (RPPA) performance and analysis

Following the indicated procedure described above, cells cultured in 10cm dishes were incubated on ice with 300uL of lysis buffer (1% Triton X-100, 50mM HEPES pH=7.5, 150mM NaCl, 1.5mM MgCl2, 1mM EGTA, 100mM NaF, 10mM Na pyrophosphate, 1mM Na3VO4 and 10% glycerol) for 20 minutes with occasional shaking every 5 min. After incubation, cells were scraped off the plate and centrifuged at 14000 rpm for 10 minutes at 4ºC. Total protein was quantified with Bradford assay and 90ug of protein was diluted 3:1 in SDS sample buffer (40% glycerol, 8% SDS, 0.25M Tris-HCl and 10% B-mercaptoethanol). Lysates were boiled at 95ºC for 5 minutes and stored at -80ºC. RPPA data was generated and analyzed by the CCSG-supported RPPA Core Facility at the University of Texas MD Anderson Cancer Center (Akbani et al., 2014). A total of 240 authenticated Antibodies for total protein expression and 64 antibodies for protein phosphorylation were analyzed in this study. The complete antibody list can be found in https://goo.gl/XKsv6s.

Gene set enrichment analysis (GSEA):

Genes were ranked according to the fold-change and p-value obtained on the differential gene expression analysis as described in (Plaisier et al., 2010). Pre-ranked files were built up for the RNA-Seq and for Chicas et al. (Chicas et al., 2010) data set and used to run a Gene Set Enrichment Analysis (GSEA) (Subramanian et al., 2005) under predefined parameters. Expression dataset files (.cls) and phenotype label files (.cls) were generated for Kabbarah (Kabbarah et al., 2010) and Talantov (Talantov et al., 2005) data sets, as well as for RPPA protein expression normalized values. GSEA was run under the following parameters: 1000 permutations, weighted enrichment analysis, signal to noise metric for ranking genes, and meandiv normalization mode. Genes with p-value ≤ 0.05 and a q-value ≤ 0.25 were considered significant.

Polysome fractionation:

Eight culture plates per condition (~23 million cells per condition) were incubated with harringtonine (2μg/mL) for 2 minutes at 37ºC followed by 5 minutes of cycloheximide (100μg/mL) treatment at 37ºC. Cells were washed twice with PBS after each treatment. Cells were scraped in 600uL of lysis buffer (50mM HEPES, 75mM KCl, 5mM MgCl2, 250mM sucrose, 0.1mg/mL cycloheximide, 2mM DTT, 1% Triton X-100 and 1.3% sodium deoxycholate and 5μl of RNase OUT) on ice. Lysates were rocked for 10 minutes at 4ºC and centrifuged at 3000g for 15 minutes at 4ºC. 400μl of lysates supernatant (cytosolic cell extracts) were layered over cold sucrose gradients (10mM HEPES, 75mM KCl, 5mM MgCl2, 0.5mM EDTA and increasing sucrose concentrations from 20% to 47%). Gradients were centrifuged at 34,000 rpms in a Beckman SW41 rotor for 2h and 40 minutes at 4ºC. After centrifugation, low (0 to 2 ribosomes) and high (<2 ribosomes)

polysome fractions were collected in Trizol (1:1) using a density gradient fractionation system (Brandel) equipped with a UA-6 absorbance detector and a R1 fraction collector. RNA was DNase treated, cleaned, and concentrated using Zymo columns (Zymo Research, Cat# R1013).

Senescence and proliferation assays

SA-β-Gal staining was performed as previously described (Dimri et al., 1995). Cells were fixed for 5 min at room temperature in 2% formaldehyde/0.2 glutaraldehyde% in PBS. After washing the cells twice with PBS, cells were stained at 37°C overnight in a non-CO_2 incubator in staining solution (40 mM Na_2HPO_4, 150 mM NaCl, 2 mM $MgCl_2$, 5 mM $K_3Fe(CN)_6$, 5 mM $K_4Fe(CN)_6$, 1 mg/ml X-gal). Images were acquired at room temperature using an inverted microscope (Nikon Eclipse Ts2) with a 20X/0.40 objective (Nikon LWD) equipped with a camera (Nikon DS-Fi3).

For BrdU incorporation, cells on coverslips were incubated with 1uM BrdU for 30 min (IMR90, ES2, and SKMel28) or 15 min (SW620, SW480, HT-29, PATU8902, and TCCSUP). Cells were fixed for 10 min at room temperature in 4% paraformaldehyde. After washing the cells three times with PBS, cells were permeabilized with 0.2% Triton X-100 for 5 min and then postfixed with 1% PF + 0.01% Tween-20 for 30 min. After washing cells three times with PBS, cells were DNaseI treated for 10 min (DNaseI). The DNaseI reaction was stopped using 20mM EDTA. After washing cells three times with PBS, they were blocked for 5 min with 3% BSA/PBS and then incubated in anti-BrdU primary antibody in 3% BSA/PBS (1:500) at room temperature for 1 h. Cells were washed

three times and then incubated in FITC anti-Rat secondary antibody (1:1000) in 3% BSA/PBS at room temperature for 1 h. Finally, cells were incubated with 0.15 μg/ml DAPI in PBS for 1min, washed three times with PBS, mounted and sealed. Images were acquired at room temperature using a Nikon Eclipse 90i microscope with a 20x/0.17 objective (Nikon DIC N2 Plan Apo) equipped with a CoolSNAP Photometrics camera.

For colony formation, an equal number of cells were seeded in 6-well plates and cultured for an additional 2 weeks. Colony formation was visualized by fixing the plates for 5 min with 1% paraformaldehyde after which they were stained with 0.05% crystal violet. Wells were destained using 10% acetic acid. Absorbance (590nm) was measured using a spectrophotometer (Spectra Max 190).

Immunofluorescence

Cells were fixed for 10 min at room temperature in 4% paraformaldehyde. After washing the cells three times with PBS, cells were permeabilized with 0.2% Triton X-100 for 5 min and then postfixed with 1% PF + 0.01% Tween-20 for 30 min. After washing cells three times with PBS cells were blocked for 5 min with 3% BSA/PBS and then incubated with the corresponding primary antibodies: anti-TSC1 (1/500), anti-ATR (1/500) anti-mTOR (1/200), anti-LAMP2 (1/100) in 3% BSA/PBS at room temperature for 1 h. Cells were washed three times and then incubated in FITC anti-Rabbit (1/2000) or Cy3 anti-mouse (1/5000) secondary antibody in 3% BSA/PBS at room temperature for 1 h. Finally, cells were incubated with 0.15 μg/ml DAPI in PBS for 1min, washed three times with PBS,

mounted and sealed. Images were acquired at room temperature using a confocal microscope (Leica SP8) with a 64X oil objective.

Western blotting

Cells lysates were collected in 1X sample buffer (2% SDS, 10% glycerol, 0.01% bromophenol blue, 62.5mM Tris, pH 6.8, 0.1M DTT) and boiled to 95°C for 10 min. Protein concentration was determined using the Bradford assay. An equal amount of total protein was resolved using SDS-PAGE gels and transferred to nitrocellulose membranes (Fisher Scientific) at 110mA for 2 h at 4°C. Membranes were blocked with 5% nonfat milk or 4% BSA in TBS containing 0.1% Tween-20 (TBS-T) for 1 h at room temperature. Membranes were incubated overnight at 4°C in primary antibodies in 4% BSA/TBS + 0.025% sodium azide. Membranes were washed 4 times in TBS-T for 5 min at room temperature after which they were incubated with HRP-conjugated secondary antibodies (Cell Signaling, Danvers, MA) for 1 h at room temperature. After washing 4 times in TBS-T for 5 min at room temperature, proteins were visualized on film after incubation with SuperSignal West Pico PLUS Chemiluminescent Substrate (ThermoFisher, Waltham, MA).

Nucleotide Analysis by LC-HRMS

Standards for ADP, dADP, dATP, dTDP, dTTP, CDP, dCDP, CTP, and dCTP and were from Sigma-Aldrich (St Louis, MO). Stable isotope labeled internal standards AMP-$^{13}C_{10}$,$^{15}N_5$, dAMP-$^{13}C_{10}$,$^{15}N_5$, ATP-$^{13}C_{10}$,$^{15}N_5$, dATP-$^{13}C_{10}$,$^{15}N_5$, dTMP-$^{13}C_{10}$,$^{15}N_2$, dTTP-$^{13}C_{10}$,$^{15}N_2$, dCMP-$^{13}C_9$,$^{15}N_3$, CTP-$^{13}C_9$,$^{15}N_3$, dCTP-$^{13}C_9$,$^{15}N_3$, were also from Sigma-Aldrich. No suitable source of stable isotope labeled ADP, dADP, dTDP, GDP, dGDP,

CDP, or dCDP was found, thus the mono-phosphate was used as a surrogate internal standard. Diisopropylethylamine (DIPEA) and 1,1,1,3,3,3-hexafluoro 2-propanol (HFIP) were purchased from Sigma-Aldrich. Optima LC-MS grade water, methanol, and acetonitrile (ACN) were purchased from Thermo Fisher Scientific (Waltham, MA).

LC-HRMS for nucleotides and other polar metabolites was as previously described (Guo et al., 2016; Kuskovsky et al., 2018). Briefly, an Ultimate 3000 UHPLC equipped with a refrigerated autosampler (at 6 °C) and a column heater (at 55 °C) with a HSS C18 column (2.1 × 100 mm i.d., 3.5 µm; Waters, Milford, MA) was used for separations. Solvent A was 5 mM DIPEA and 200 mM HFIP and solvent B was methanol with 5 mM DIPEA 200 mM HFIP. The gradient was as follows: 100 % A for 3 min at 0.18 mL/min, 100 % A at 6 min with 0.2 mL/min, 98 % A at 8 min with 0.2 mL/min, 86 % A at 12 min with 0.2 mL/min, 40 % A at 16 min and 1 % A at 17.9 min-18.5 min with 0.3 mL/min then increased to 0.4 mL/min until 20 min. Flow was ramped down to 0.18 mL/min back to 100 % A over a 5 min re-equilibration. For MS analysis, the UHPLC was coupled to a Q Exactive HF mass spectrometer (Thermo Scientific, San Jose, CA, USA) equipped with a HESI II source operating in negative mode. The operating conditions were as follows: spray voltage 4000 V; vaporizer temperature 200 °C; capillary temperature 350 °C; S-lens 60; in-source CID 1.0 eV, resolution 60,000. The sheath gas (nitrogen) and auxiliary gas (nitrogen) pressures were 45 and 10 (arbitrary units), respectively. Single ion monitoring (SIM) windows were acquired around the $[M-H]^-$ of each analyte with a 20 *m/z* isolation window, 4 *m/z* isolation window offset, $1e^6$ ACG target and 80 ms IT, alternating in a Full MS scan from 70-950 *m/z* with 1e6 ACG, and 100 ms IT. Data was analyzed in XCalibur v4.0

and/or Tracefinder v4.1 (Thermo) using a 5 ppm window for integration of the peak area of all analytes.

Glucose labeling and analysis

Cells were seeded in 10 cm culture plates, and at the end of the indicated treatment media was replaced by 6mL of DMEM (Cat# D5030) supplemented with 0.5% of charcoal stripped FBS, 5mM of $^{13}C_6$-D-glucose and 20mM of HEPES. After 8 hours cells were harvested and snap frozen in liquid nitrogen.

Isotopologue patterns for dNDPs, dNTPs and ribose-5-phosphate were analyzed by LC-HRMS as indicated above. Adjustment for natural isotopic abundance was conducted through open source and publicly available FluxFix (Trefely et al., 2016).

Flexible Flow Cytometry System (FACS)

Cells were washed and pelleted in PBS by centrifugation at 1000 rpm for 5 minutes. Cells were fixed in cold ethanol (70%) while vortexing and spun down at 4000 rpm for 15 minutes at 4ºC. Rapidly, cells were resuspended in propidium iodide staining solution (69uM propidium iodide, 38mM NaCitrate and 19ug/mL RNAse A) and incubated at 37ºC for 30 minutes. Stained cells were run on a 10-color FACSCanto flow cytometer (BD biosciences). Data were analyzed with FlowJo Software.

RT-qPCR

Total RNA was extracted from cells with Trizol and DNase treated, cleaned, and concentrated using Zymo columns (Zymo Research, Cat# R1013) following manufacturer's instructions. Total RNA was extracted from tissues with NucleoSpin RNA/Protein (Macherey-Nagel, Cat#740933) following manufacturer's instructions. Optical density values of extracted RNA were measured using NanoDrop One (Thermo Scientific) to confirm an A260 and A280 ratios above 1.9. Relative expression of target genes (listed in **Table S5**) were analyzed using the QuantStudio 3 Real-Time PCR System (Thermo Fisher Scientific) with clear 96 well plates (Greiner Bio-one, Cat#652240). Primers were designed using the Integrated DNA Technologies (IDT) tool (http://eu.idtdna.com/scitools/Applications/RealTimePCR/) (**Table S5**). Briefly, 25ng of total RNA was used to One-Step qPCR (Quanta BioSciences, Cat# 95089) following manufacturer's instruction in a final volume of 10uL. Conditions for amplification were: 10 min at 48ºC, 5 min at 95ºC, 40 cycles of 10 s at 95ºC and 7 s at the corresponding annealing temperature (**Table S5**). The assay ended with a melting-curve program: 15 s at 95ºC, 1 min at 70ºC, then ramping to 95ºC while continuously monitoring fluorescence. Alternatively, relative expression of the low abundant *CDKN2A* was determined following and adaptation of Zhang Q, et al. TqPCR method (Zhang et al., 2015). Conditions for amplification were: 10 min at 48ºC, 5 min at 95ºC, 4 cycles of 10s at 95ºC and 10s starting at 66ºC and decreasing 2ºC per cycle, 40 cycles of 10 s at 95ºC and 7 s at 64ºC. The assay ended with a melting-curve program: 15 s at 95ºC, 1 min at 70ºC, then ramping to 95ºC while continuously monitoring fluorescence. Each sample was assessed in triplicate. Relative quantification was determined to multiple reference genes (*B2M*, *MRPL9*, *PSMC4* and *PUM1*) using the delta-delta Ct method.

Murine tumor model

HT-29 colorectal carcinoma cells were infected with shRNA targeting p16 and RPIA alone or in combination. After 2 days of puromycin selection (3μg/mL), 3 million cells were resuspended in 200μl of PBS and injected subcutaneously into the left flank of SCID mice. Mice were monitored daily to identify palpable tumors. Mice weight and tumor length (L) and width (W) (L>W) were measured every 3 days after a tumor volume of 200mm^3. Tumor volume was calculated as ½ (L x W^2). All animals were sacrificed at day 26 post injection and tumor tissues collected for following experiments.

Quantification and Statistical Analysis

GraphPad Prism version 7.0 was used to perform statistical analysis. The appropriate statistical test was used as indicated to determine p values of raw data. P-values < 0.05 were considered significant. Survival plots were performed in GraphPad Prism version 7.0. Data for the indicated tumors was obtained from cBioportal (Cerami et al., 2012; Gao et al., 2013). Longitudinal and cross-sectional analysis of tumor volume where calculated using TumorGrowth tool using default parameters (Enot et al., 2018).

Supplemental Tables

Table S1: Gene sets positively upregulated in senescence bypass cells by GSEA; related to Figure 2.

Table S2: Gene sets positively upregulated in RAS/shpRB by GSEA in Chicas et al. data set; related to Figure 2.

Table S3: qPCR expression analysis for the heavy and light polysome fractions; related to Figure 5.

Table S4: Leading-edge genes associated with "translation" and "DNA repair" in senescence versus senescence bypass GSEA used for survival analysis; related to Figure 4.

Table S5: Primers used for these studies.